Systematic Check of Blowfish Neutron Detector for GDH Experiment: with an emphasis on gain calibration

A Thesis Submitted to the

College of Graduate and Postdoctoral Studies

in Partial Fulfillment of the Requirements

for the degree of Master of Science

in the Department of Physics and Engineering Physics

University of Saskatchewan

Saskatoon

By

Meena Sharma

Permission to Use

In presenting this thesis in partial fulfilment of the requirements for a Postgraduate degree from the University of Saskatchewan, I agree that the Libraries of this University may make it freely available for inspection. I further agree that permission for copying of this thesis in any manner, in whole or in part, for scholarly purposes may be granted by the professor or professors who supervised my thesis work or, in their absence, by the Head of the Department or the Dean of the College in which my thesis work was done. It is understood that any copying or publication or use of this thesis or parts thereof for financial gain shall not be allowed without my written permission. It is also understood that due recognition shall be given to me and to the University of Saskatchewan in any scholarly use which may be made of any material in my thesis.

Requests for permission to copy or to make other use of material in this thesis in whole or part should be addressed to:

Head of the Department of Physics and Engineering Physics

116 Science Place

University of Saskatchewan

Saskatoon, Saskatchewan S7N 5E2

Canada

OR

Dean

College of Graduate and Postdoctoral Studies

University of Saskatchewan

116 Thorvaldson Building, 110 Science Place

Saskatoon, Saskatchewan S7N 5C9

Canada

ABSTRACT

The University of Saskatchewan subatomic physics group, along with collaborators from the University of Virginia, Duke University and others, are preparing to measure the low-energy regime of the Gerasimov-Drell-Hearn (GDH) sum rule for the deuteron. This sum rule connects an energy weighted integral of spin-polarized photo-absorption cross sections with the anomalous magnetic moment of the target. It is based on the gauge and Lorentz invariance, and the general principles of causality and unitarity. The measurements made for the GDH sum rule will use the *Blowfish* neutron detector to detect the neutrons following the deuteron photodisintegration. The GDH sum depends on the difference between absolute cross sections. It is therefore critical to the success of the measurement that systematic uncertainties, in the determination of the absolute cross sections, are understood. This MSc thesis will include a thorough investigation of the systematic uncertainties in the measurement. This will include: verification of the gain monitoring system for the *Blowfish* neutron detector cells; verification of the photon flux monitor; and the calibration of that system.

ACKNOWLEDGEMENTS

DEDICATION

ਗੁਰੂ ਦੀ ਕਿਰਪਾ ਨਾਲ

CONTENTS

List of Tables

LIST OF FIGURES

LIST OF ABBREVIATIONS

ADC   Analogue to Digital Converter
AmBe   Americium-Beryllium neutron source
BC-400   Bicron-400 solid organic scintillator
BC-505   Bicron-505 liquid organic scintillator
DAQ   Data Acquisition System
DFELL   Duke Free Electron Laser Laboratory
DNP   Dynamic Nuclear Polarization
FEL   Free Electron Laser
GDH   Gerasimov-Drell-Hearn
GEANT4   Geometry And Tracking, Version 4
HIGS   High Intensity Gamma Source
HIFROST   HIGS Frozen Spin Polarized Target
LED   Light Emitting Diode
NMR   Nuclear Magnetic Resonance
OK   Optical Klystron
PMT   Photomultiplier Tube
PSD   Pulse Shape Discrimination
TDC   Time-to-Digital Converter
ToF   Time of Flight
TUNL   Triangle University Nuclear Laboratory

Chapter 1

Introduction

A deuteron, the ^{2}H nucleus, consists of a neutron and a proton; the neutral atom is called deuterium. It is the simplest bound state of nucleons and therefore gives us an ideal system for studying the nucleon-nucleon interaction.

Nucleon scattering experiments are one way to study the nucleon-nucleon interaction. If the target is a nucleus with many nucleons, the observed scattering of a single nucleon will include the complicating effects of multiple encounters, making it very difficult to extract information about the nucleon-nucleon interaction.

Photodisintegration of a deuteron is when the neutron and proton break apart after the absorption of a high energy photon. The probability of the neutron and proton breaking apart is characterized by the photodisintegration cross section, which depends on the incoming photon energy. The photodisintegration reaction provides an ideal testing ground for the nucleon-nucleon interaction. Because the reaction is initiated by a photon, and the electromagnetic interaction is well understood, the calculation of the photodisintegration cross section using a model of the nucleon-nucleon interaction is simplified.

1.1 Gerasimov-Drell-Hearn Sum Rule

The deuteron also provides a testing ground for fundamental principles of physics. In addition to its dependence on photon energy, the photodisintegration cross section may also depend on the relative orientations of the target spin and the helicity of the incoming photon. Helicity is a property that characterizes the relative orientation of a particle's spin vector ($\mathbf{s}$) with

respect to its momentum vector ($\mathbf{p}$). Helicity is defined as,

$$h = \frac{\mathbf{s} \cdot \mathbf{p}}{|\mathbf{s} \cdot \mathbf{p}|}.$$

The helicity, h, then yields a value of $+1$, for a spin vector parallel to the momentum vectors; and -1, for a spin vector antiparallel to the momentum vector [Kra88].

The Gerasimov-Drell-Hearn (GDH) sum rule is rooted in fundamental principles, such as causality, unitarity, and gauge and Lorentz invariance. For a circularly polarized photon of energy ν; the GDH sum rule is given by,

$$\int_0^\infty (\sigma^P(\nu) - \sigma^A(\nu)) \frac{d\nu}{\nu} = 2\pi^2 \alpha S_t \left(\frac{\kappa_t}{M_t} \right)^2, \tag{1.1}$$

where $\sigma^P(\nu)$ and $\sigma^A(\nu)$ are the total photodisintegration cross sections with the target spin and the circularly polarized photon helicity are parallel (P) and anti-parallel (A), α is the fine structure constant, κ_t is the anomalous magnetic moment of the target, M_t is the mass of the target, and S_t is the target spin [DH66, Ger66].

For a nucleon, the photodisintegration cross section is zero below the pion production threshold (~ 140 MeV); but for the deuteron, the photodisintegration threshold is low (2.22 MeV). It is predicted that there is a very large contribution to the GDH integral for the deuteron at low energies (particularly below about 20 MeV)[Saw05]. Our group is planning to measure the GDH integrand at low energies.

This low-energy measurement uses the *Blowfish* neutron detector to detect the neutrons following deuteron photodisintegration. The target will be a cryogenic target, which insures the deuteron spin direction is fixed. The GDH integrand depends on the difference between absolute cross sections, $\sigma^P - \sigma^A$. It is, therefore, critical to the success of the measurement that systematic uncertainties, in the determination of the absolute cross sections, are understood and controlled.

1.2 Nuclear Reaction Measurements

For the deuteron photodisintegration reaction the reaction products are a neutron and a proton. We choose to detect to outgoing neutron. Protons, having a charge, do not travel

far in materials, and therefore would be difficult to detect, especially at low energies. Neutrons, being electrically neutral, do not interact strongly with materials. This allows us to have larger targets, which increases the number of target nuclei. Also, neutrons are able to penetrate a target containment vessel, such as necessary for the cryogenic target needed for the GDH experiment.

However, because neutrons are electrically neutral, and do not interact electromagnetically, they are more difficult to detect. Therefore, detecting neutrons relies on detecting secondary charged particles produced by nuclear reactions. For our experimental situation the preferred nuclear reaction is neutron elastic scattering. Elastic scattering conserves kinetic energy in the centre of mass frame. We detect the neutron by detecting a recoiling charged particle following neutron scattering.

We need to relate the number of neutrons detected to the differential cross section for the photodisintegration reaction.

The cross section characterizes the probability of reactions between an incident flux of particles and the target nucleus; the differential cross section for a reaction is a function of the incident particle energy and a reaction product direction characterized by the angles θ and ϕ, where θ and ϕ are defined in figure 1.1. For our experiments the beam line, or incident photon direction, is chosen to be along the z-axis.

The total cross section, $\sigma(E)$, for a given incident particle of energy E, is related to the differential cross section by

$$\sigma(E) = \int d\Omega \frac{d\sigma(E, \theta, \phi)}{d\Omega}, \tag{1.2}$$

where $\frac{d\sigma(E,\theta,\phi)}{d\Omega}$ is the differential cross section.

The number of reaction product particles, N_s, in the limit of a thin target of thickness δz, scattered into the solid angle, $\Delta\Omega$, is related to the differential cross section by,

$$N_s = N_{tot} n \delta z \frac{d\sigma}{d\Omega} \Delta\Omega, \tag{1.3}$$

where N_{tot} is the total number of incident particles, n is the density of the targets centres, and δz is the target thickness along the beam axis. Then, the number of detected product particles, in a detector subtending solid angle $\Delta\Omega$ is given by,

$$N_D = \epsilon N_s, \tag{1.4}$$

3
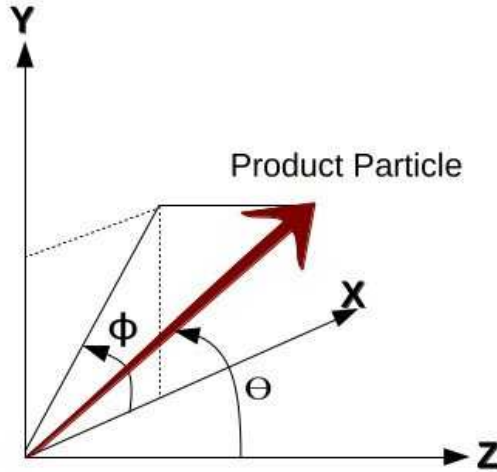
Figure 1.1: The Cartesian coordinate orientation for the GDH experiment; where the z-direction is the incident beam direction.

where ϵ is the efficiency at which the neutrons can be detected. The efficiency, ϵ, depends on the geometry of the experiment and the intrinsic efficiency of the detector.

In order to extract differential cross-sections we need to know the efficiency, ϵ, and the number of incident photons. In our experiments the number of incident photons is measured using the 5-paddle flux monitor. The detector efficiency is calculated using a simulation of the detector system. The detector systems will be discussed, in detail, in chapter 2.

1.3 *Blowfish* Detector

Blowfish is a neutron detector; it is composed of an array of 88 detector cells, which covers a solid angle of about $\frac{1}{4}$ of 4π steradian. The detector cells are arranged on 8 uniformly spaced arms, which can rotate about the conventional beam axis in the ϕ direction. Each arm contains 11 uniformly spaced cells on the surface of a 16 inch radius sphere covering polar angles from $\theta = 22.5°$ to $\theta = 157.5°$. The array's large solid angle coverage makes it ideal for few-body experiments, where it is important to measure the angular distribution of reaction products. The fact that the array can be rotated about the beam axis allows for accurate determination of any systematic effects in the detector efficiency. Figure 1.2 depicts
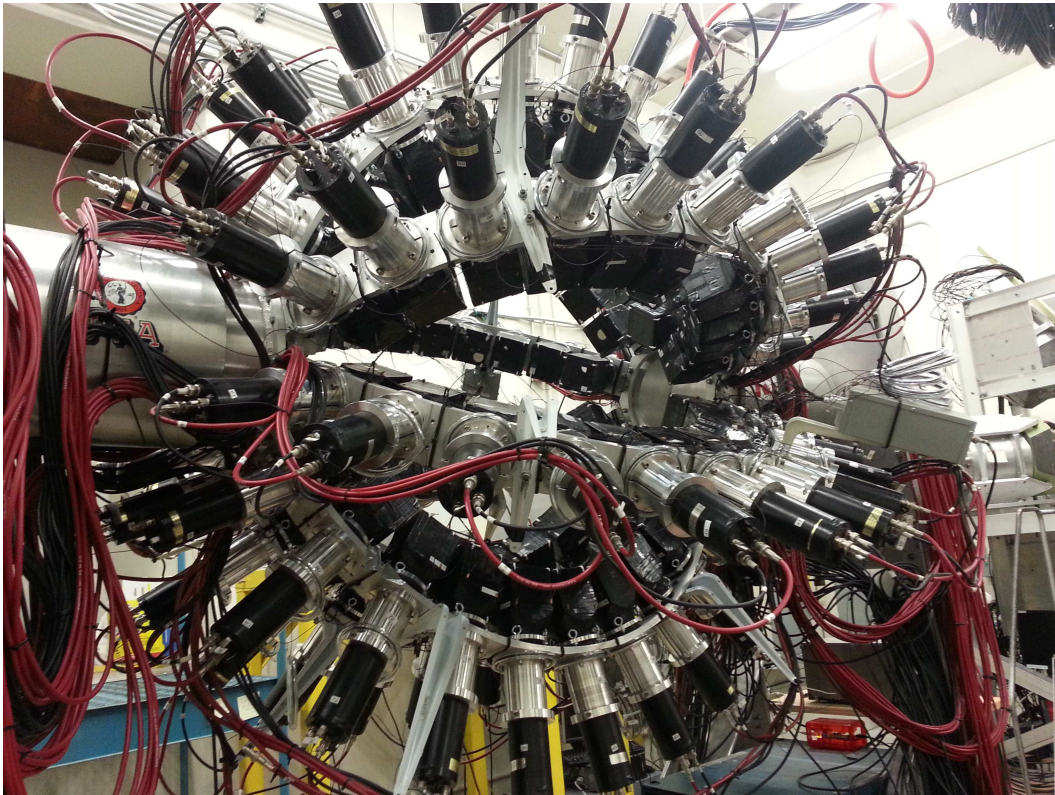
Figure 1.2: The *Blowfish* neutron detector. Picture taken at the HIGS facility in September 2013.

the newly updated *Blowfish* detector.

Normally the reaction target is placed at the centre of *Blowfish* and the incident photon beam is coincident with the rotation axis of *Blowfish* (the $z-$axis). For the GDH measurement however, *Blowfish* is rotated 90° about the vertical axis to accommodate the insertion of the cryogenic target.

1.4   Detector Efficiency and Gain

As mentioned above, the number of detected product particles, N_D is dependent on the efficiency of the detector. A significant factor contributing to the efficiency is the fact that not all neutrons that interact in a detector can be counted. In a practical detector only output signals that are larger than some minimum value, known as a threshold, are counted. Signals smaller than the threshold are not counted.

We detect neutrons by detecting a recoil charged particle following elastic scattering of the neutron. The recoil charge particle can have any energy ranging from zero up to the energy of the incident neutron, depending of the scattering angle. Therefore, not all neutrons that interact in the detector will have a large enough output signal to be above the detector's threshold, and therefore be counted.

The output response of a detector can be calibrated in energy units, known as the light output. The light output is related to the energy deposited in the detector by an incident particle. The relation between the signal from a detector and the light output is characterized by a quantity known as the gain. Figure 1.3 shows a sketch of the light output spectrum from a detector for a given incident neutron energy. If the threshold is at the indicated light output only neutrons in the cross-hatched area will be counted. Therefore if the efficiency of the detector for detecting neutrons is to be determined, it is important to know where the threshold is in relation to the light output response of the detector, which in turn depends on the gain. An uncertainty in the gain leads to an uncertainty δE_T in the threshold E_T which results in an uncertainty in the detector efficiency.

Therefore, an accurate knowledge of the gain is needed to determine the efficiency of our detector system, which is important for accurate cross section measurements. This thesis
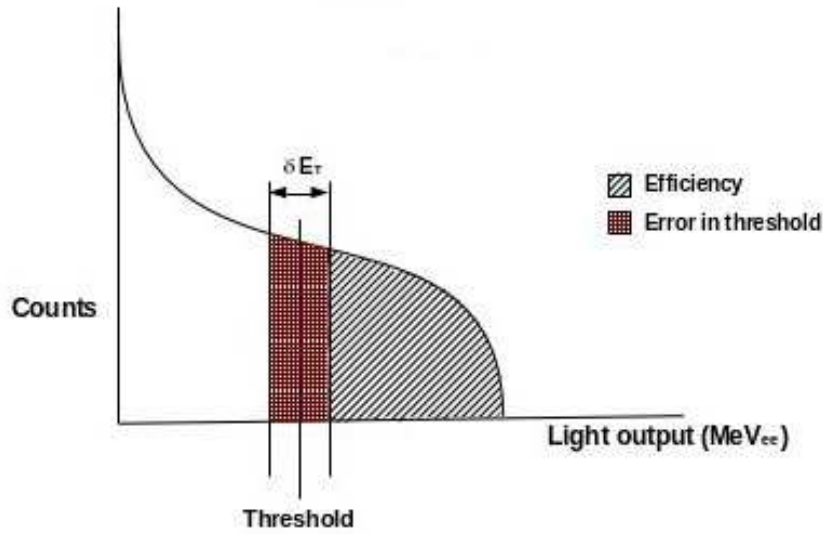
Figure 1.3: A sketch of the light output spectrum from a detector, for a given incident neutron energy. Only signals from the detector that are above a given threshold energy, E_T, can be counted. The δE_t is the error in determining the threshold energy.

is concerned with measurements designed to determine how accurately we can measure the gain of the detector cells that make up the *Blowfish* neutron detector.

1.5 Outline

This thesis will start by discussing particle detection, via scintillators; this leads to the specifications of the *Blowfish* detector and the experimental set up for the GDH experiment; then the relationship between the detector efficiency and the gain is explained. Next, this thesis will provide more details about the gain calibration procedure, the gain monitoring system, and the experimental impact of the gain. This leads to the experimental results of this thesis; starting with the specifics of the data collection, and leading into the data analysis needed to determine the gain of each detector cell. These gains will be analysed to check the gain stability, and check the gain tracking system and the predictability of the gain. The thesis will then look into the effect of a gain error on the uncertainty associated with determining the neutron yield using the *Blowfish* detector for the case of deuteron

photodisintegration in the GDH experiment. This thesis concludes with a summation of our results, and the remaining tasks left before performing the GDH experiment.

Chapter 2
Experimental Equipment

This section will describe the experimental components necessary for making cross section and differential cross section measurements for photoneutron reactions. As mentioned in the previous chapter we use the *Blowfish* neutron detector array to measure the outgoing neutrons. The detector cells within *Blowfish* detect neutrons by the indirect method of neutron elastic scattering giving rise to a recoil charged particle.

We begin with a general discussion of the principles involved in particle detection.

2.1 Particle Detection

All the particle detectors used in the experiments discussed in this thesis are of a class known as scintillation detectors or scintillators.

2.1.1 Scintillators

Generally, scintillators absorb the kinetic energy of the incoming particle, and via the Coulomb interaction, it converts this kinetic energy into detectable light.

Charged particles will interact directly with the atomic electrons of the scintillator. Gamma rays interact with the atomic electrons by Compton scattering, the photoelectric effect, or by pair production. The energy is transferred to an electron or positron, which then deposits energy in the detector by Coulomb interactions with other atomic electrons.

Neutrons in a hydrogen rich detector will most likely collide with a proton, or it can scatter off a heavier nucleus. That recoil proton, or nucleus, will travel through the detector cell depositing its kinetic energy through the Coulomb interaction.

9

In our experimental set up, scintillators are used in the five-paddle flux monitor and the *Blowfish* neutron detector. The five-paddle flux monitor utilizes a solid organic scintillator, with the brand name BC-400, and the *Blowfish* neutron detector utilizes a liquid organic scintillator, with the brand name BC-505. Solid organic scintillators are proportionally inexpensive and can be formed into versatile shapes, with a large size range. Liquid organic scintillators tend to have a higher light output [Kno10]. The liquid organic scintillator chosen for the *Blowfish* cells has a special property that allows us to tell the difference between energy deposited by electrons or by heavier charged particles (see section 2.2.2).

In all of these cases, charged particles leave atomic electrons in excited states or it ionizes the atom. The subsequent de-excitations of these atoms produces the scintillation light, which is guided to a photomultiplier tube (PMT) for amplification [Bew05].

2.1.2 Photomultiplier Tubes

The scintillated light is directed to the photocathode of the the photomultiplier tube; the common acronym for photomultiplier tube is PMT. The photocathode uses the photoelectric effect to convert light from the scintillator into a current of electrons. The photoelectric effect is described by Einstein's formula,

$$E = h\nu - \phi, \tag{2.1}$$

where E is the photoelectron's kinetic energy, ν is the frequency of the impacting scintillation light, and ϕ is the work function of the photocathode material. In accordance with this formula, the scintillator chosen must emit light with an energy above the work function of the photocathode, ϕ.

The photoelectron are then accelerated through a potential difference and then hit a dynode where more electrons are knocked out. Thus the electron current is boosted. Figure 2.1 is a simplified depiction of the electron current being multiplied by a series of dynodes. As the electrons are accelerated from one dynode to the next more secondary electrons are emitted; these secondary electrons are accelerated to the next dynode causing a further multiplication of electrons; this effect is referred to as cascading. This electron cascade is then collected at the anode; where the electron cascade, or current, is passed on to the data
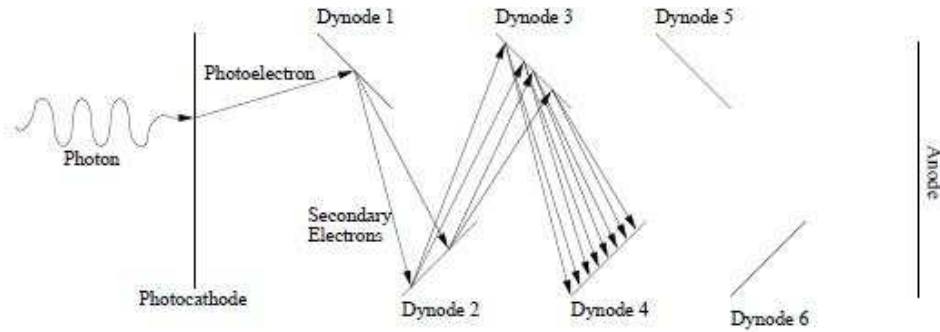
Figure 2.1: Equivocal design of the photomultiplier tube; a sketch of how a photon signal is amplified dynode-to-dynode (image credit: [Wur10]).

acquisition system [Bew05].

The collection and multiplication of the scintillation light in the PMT is made possible by the high-voltage supply attached to *Blowfish*. This external high-voltage source is connected to the PMTs; the high-voltage connection is done in a way that the photocathode and each of the following dynode stages are correctly biased with respect to one another. The voltage between the photocathode and the first dynode is several times greater than the dynode-to-dynode voltage difference [Kno10]. The supplied voltage is equally split between the remaining dynodes.

The high-voltage setting is very important to the functionality of the PMT. A variation in the applied voltage can lead to gain changes due to the resulting changes in the dynode potentials. The gain of a PMT is also sensitive to changes in temperature. For this reason it is usual to wait for some time after turning on the high voltage to a PMT before measurements are made. This is to allow it to reach its operating temperature and for its gain to stabilize. Another possible cause of gain changes is when there are large changes in the counting rate experienced by the PMT; this effect is referred to as fatigue. However, for the PMT model used in the *Blowfish* detector, a Phillips XP2262B twelve stage photomultiplier tube, the gain drift due to fatigue, is expected to be under 1% error to the gain value. As a PMT ages its gain can also change.

Since PMT gain changes can occur, the gain of the detector system must be periodically measured. This is done using a known energy radioactive source [Bew05].

Figure 2.2 shows how each individual *Blowfish* detector is assembled; the cell contains the
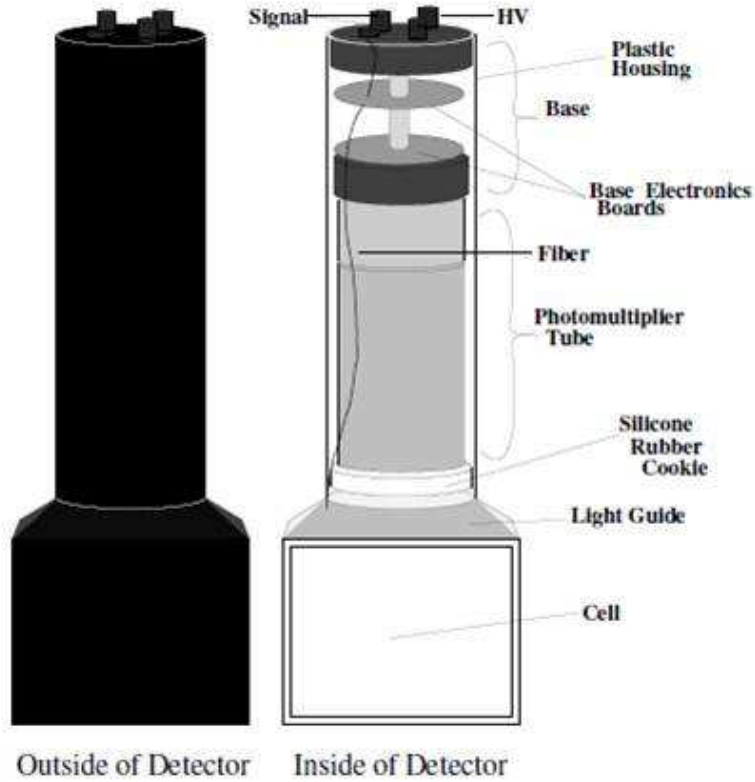
Figure 2.2: A diagram of an individual *Blowfish* detector (image credit: B.Bewer [Bew05]).

liquid scintillator BC-505. A detailed description of the detector is given in section 2.2.

The output current pulse from the PMT will be sent to an analog-to-digital converter (ADC) where the integral of the pulse will be converted to a number to be read by a data acquisition system.

2.1.3 Light Output

The correlation between the scintillator light output and the particle energy is not linear. The light output is not directly related to the energy deposited into the scintillator; however, the light output is related to the type and energy of the particle causing the light emittance. The function that describes the relation between the light output and the energy deposited into the BC-505 liquid scintillator was explored by Pywell et al. in [PSI+06]. A general

expression of the light output function is,

$$\frac{dL}{dx} = Sf\left(\frac{dE}{dx}\right),$$ (2.2)

where $\frac{dL}{dx}$ is the differential light output, as the particle traverses a distance x through the material; the energy loss is represented by $\frac{dE}{dx}$; S is the scaling parameter related to the absolute scintillation efficiency. and f is a function that describes the relationship between $\frac{dL}{dx}$ and $\frac{dE}{dx}$.

Under the condition where a particle, of energy E, stops in the scintillator, in a range of R, the total light output $(L(E))$ is,

$$L(E) = \int_0^R \frac{dL}{dx}dx = S \int_0^R f\left(\frac{dE}{dx}\right)dx.$$ (2.3)

In order to circumvent the complications associated with determining the absolute scintillation efficiency, S, the light output is given in terms of the equivalent electron energy (MeV_{ee}); the equivalent electron energy is the energy of an electron that gives the same light output. This simplification is possible because the energy deposited by an electron is linearly related to its light output.

So the light output, $L(E)$, can be written in terms of the gain, g, of the detector.

$$gA(E_e) = L(E_e) \equiv E_e,$$ (2.4)

where E_e is the electron energy with the corresponding light output $L(E_e)$; and A is the ADC channel number (the detector output) [PSI+06].

For BC-505, a best fit to light output data is found with the Chou parametrization function [Cho52]

$$f\left(\frac{dE}{dx}\right) = \frac{dE}{dx}\left[1 + kB\left(\frac{dE}{dx}\right) + C\left(\frac{dE}{dx}\right)^2\right]^{-1}$$ (2.5)

where kB and C are constants [PSI+06]. Figure 2.3 shows the light output (in equivalent electron energy MeV_{ee}) when the particle, with the given kinetic energy, stops in the BC-505 scintillator.

2.1.4 Scintillator Response to Photons

The three methods in which photons interact with matter are photoelectric absorption, Compton scattering, and pair production. The photon is completely absorbed in the case of
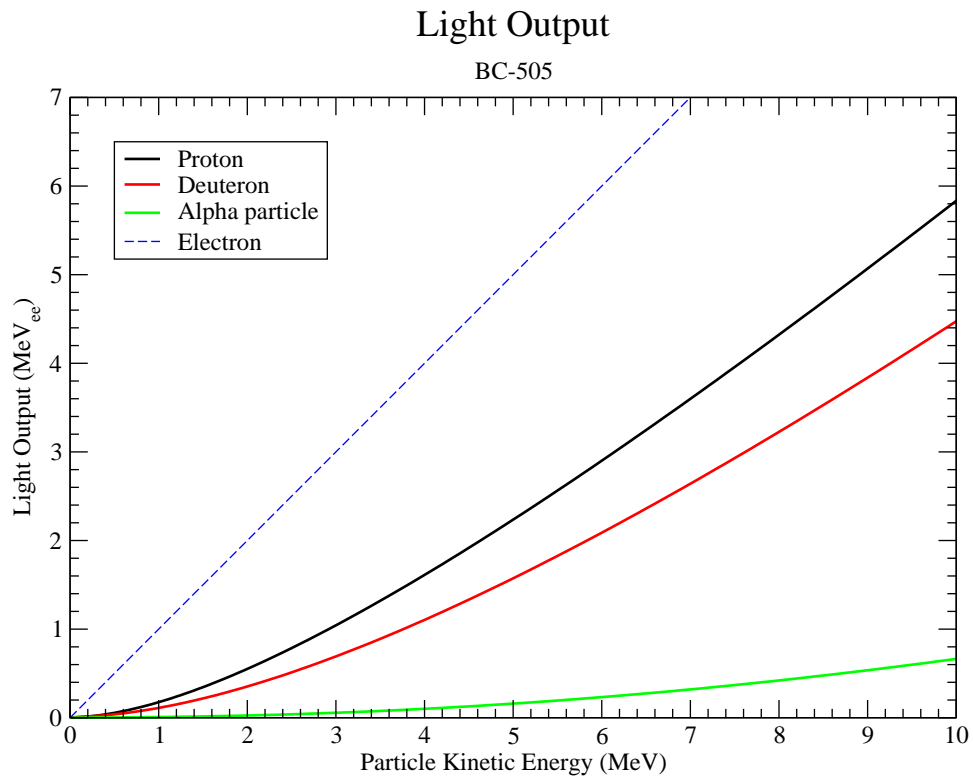
Figure 2.3: Light output response for various particles. It shows the light output (in equivalent electron energy MeV_{ee}) when the particle, with the given kinetic energy, stops in the BC-505 scintillator. (Image courtesy of Rob Pywell.)

14

the photoelectric effect, and pair production; the photon's energy is only partially absorbed in the photon's Compton scattering interaction with a scintillator.

Photoelectric Absorption

In the process of photoelectric absorption the photon completely deposits its energy into the material. In the photon's place an energetic photoelectron is ejected from its energy level in an atom; it's important to note that this form of interaction only takes place with bound electrons. The photoelectron energy, E_{e^-}, is given by the following equation:

$$E_{e^-} = h\nu - E_b,$$

where E_b represents the binding energy of the photoelectron in its pre-collision state [Kno10]. This method of interaction is favourable at lower photon energies.

Pair Production

Pair production is the process of a high energy photon creating an electron and positron, when the photon is near a nucleus. This method of photon interaction is favourable at high photon energies.

Compton Scattering

Compton scattering is the foremost interaction mechanism for gamma-ray energies of radioisotope sources. The incoming gamma-ray photon is deflected through an angle θ with respect to its original direction. The photon transfers a portion of its energy to the electron, which then is known as a recoil, or scattered, electron. Figure 2.4 is a depiction of the associated energies and angles in Compton scattering.

The corresponding equation that relates the energy transfer and scattering angle is,

$$h\nu' = \frac{h\nu}{1 + \frac{h\nu}{m_0 c^2}(1 - \cos\theta)}, \tag{2.6}$$

where $m_0 c^2$ is the rest-mass energy of the electron (0.511 MeV) [Kno10]. This method of photon interaction is most common at mid range photon energies (the energies that are experienced in these experiments).
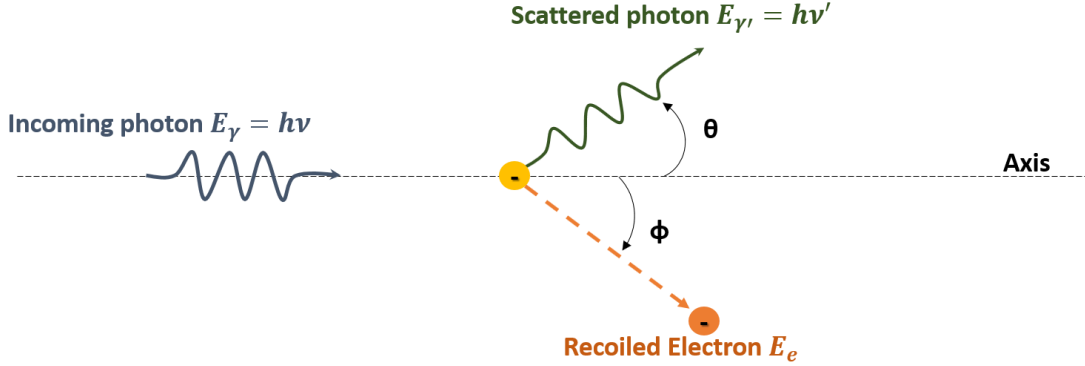
Figure 2.4: Compton scattering illustration of a photon's energy transfer to a stationary electron, and the associated scattering angles. Here, $E_\gamma = h\nu$, $E_{\gamma'} = h\nu'$, and $E_e = \sqrt{m_0{}^2 c^4 + p^2 c^2}$

2.1.5 Scintillator Response to Neutrons

The light output response to neutrons is mostly due to recoiling protons in the scintillator. Since the mass of the recoiling proton is larger than the mass of recoiling electrons or positrons (resulting from photon interactions), the proton looses energy in a shorter distance in the scintillator material. Therefore the density of energy deposited by the recoiling proton is higher than that for an electron or positron. This changes the time structure of the scintillation light produced. We make use of this difference to distinguish between neutron and photons. This is called pulse shape discrimination (PSD) and will be further discussed in section 2.2.2.

An example of the *Blowfish* detector's response to incoming neutrons is given in figure 2.5 which shows the light output spectrum when neutrons with kinetic energy 8.9 MeV are incident on a detector cell [PSI+06]. Also shown is the simulated light output spectrum which make use of the light output function for BC-505 discussed in section 2.1.3.

2.2 *Blowfish*

Blowfish is a neutron detector; composed of an array of 88 cells. Figure 2.6 shows a simulation model of *Blowfish* in its standard orientation.

The detector covers a solid angle of approximately $\frac{1}{4}$ of 4π steradian. The array's ori-
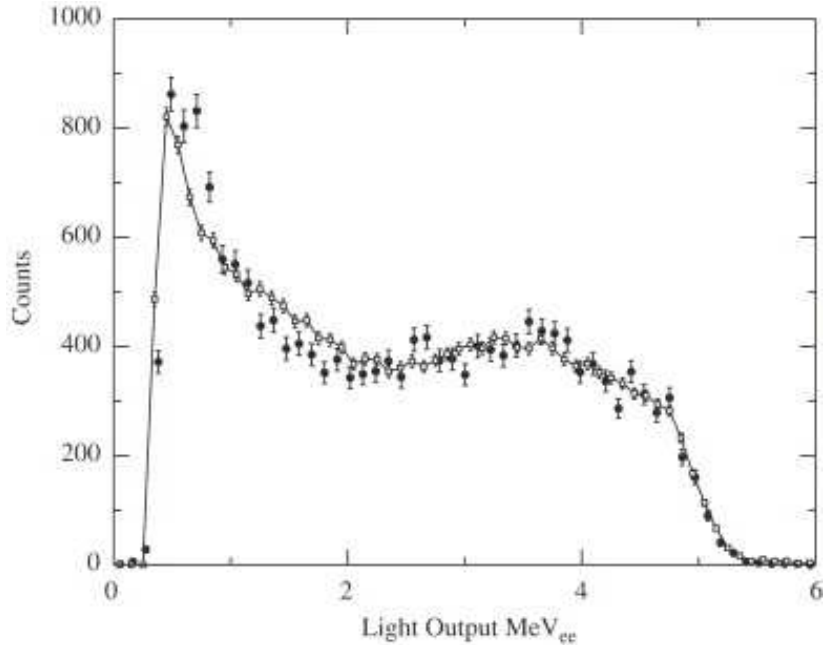
Figure 2.5: A light output spectrum for tagged 8.9 MeV neutrons; the solid circle dots are the experimental data points; and the open squares are from a GEANT4 simulation (image credit: [PSI$^+$06]).

entation is composed of 8 uniformly spaced arms, which can rotate about the conventional beam axis in the ϕ direction. Each arm is composed of 11 uniformly spaced cells on the surface of a 16 inch radius sphere covering polar angles from $\theta = 22.5°$ to $\theta = 157.5°$. The array's large solid angle coverage makes it ideal for few-body experiments, where reaction products have varying angular dependence [Wur10]. In its standard orientation it is possible to rotate *Blowfish* around the beam axis to allow the investigation of systematic effects. It is important to note that for the GDH experiment the beam line is rotated 90 degrees about the vertical axis.

The detector cells on *Blowfish* are made of three main components: a liquid organic scintillator, a light guide, and a Photomultiplier Tube (PMT) connected as shown in figure 2.2. The scintillator cell is a Lucite box with the following dimensions: 8.2 cm × 8.2 cm × 7.1 cm, with 0.3 cm thick walls. The cells are filled with BC-505 liquid scintillator. The scintillator functions as a way to convert the kinetic energy of incident particles into light. The total scintillator active volume is $7.6 \times 7.6 \times 6.5$ cm^3. Each cell is optically coupled to a 12-stage Phillips XP2262B PMT through a 4.5 cm Lucite light guide and a ≈ 0.5 cm thick silicone

17
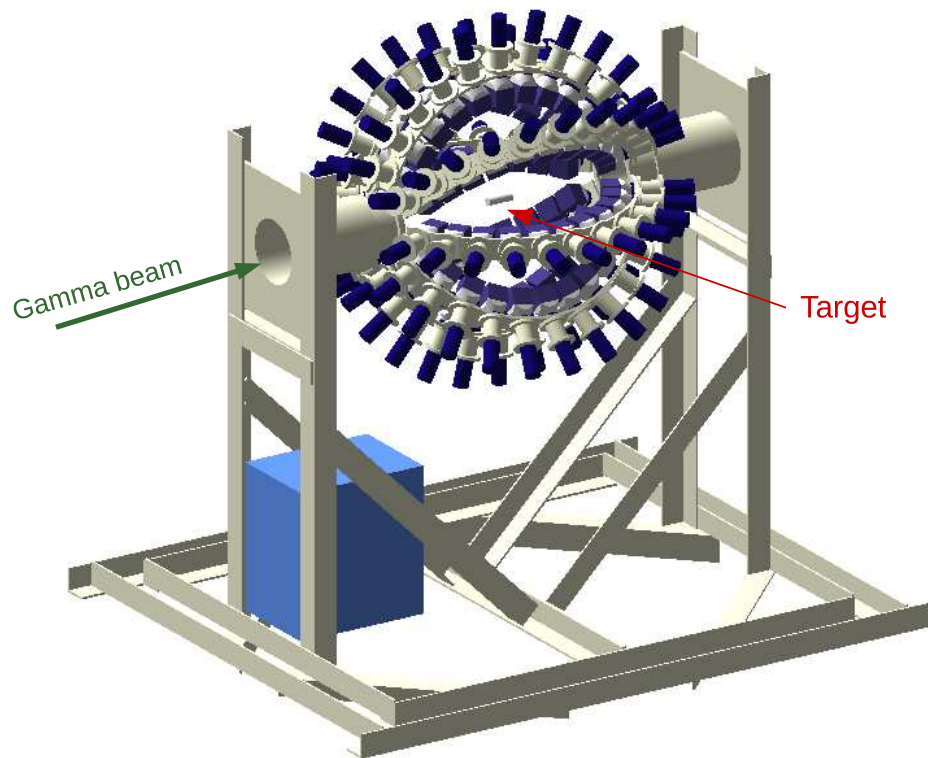
Figure 2.6: The GEANT4 simulation of *Blowfish* in the standard *Blowfish* orientation. The solid blue box is the high-voltage power supply and the grey is the aluminum mounting frame. (Image courtesy of Rob Pywell.)

"cookie". Each detector is made light tight so that only light originating in the BC-505 scintillator can reach the PMT.

Each mounted detector is connected to a high voltage source, which regulates the PMT voltages. Mounted on the *Blowfish* detector are four light-tight flasher boxes that contain light emitting diodes (LEDs) that are connected to every cell via fibre optic cables; this is referred to as the flasher system, and is going to be discussed in Chapter 3.

2.2.1 Electronics

This section will briefly describe the electronics that receive and transport the analogue signals coming in from the *Blowfish* neutron detector cells.

The analogue signals coming from each *Blowfish* cell is sent through a discriminator. A discriminator only produces a logic signal output if the amplitude of the incoming signal pulse is above a set threshold. Therefore, the discriminators reject electronic noise from the detector cells.

From the discriminator, the analog signal then passes to two analog-to-digital converters (ADCs). Each cell has a long and short-gate ADC; the long-gate ADC integrates the entire signal, and the short-gate integrates the signal over a set, shorter, time. Both ADCs are parallel to one another. Comparison of the long and short gate ADC outputs allows the particle (causing the signal) to be classified through pulse-shaped discrimination (PSD). The PSD is discussed in section 2.2.2.

The digital discriminator outputs are fed to inhibited and uninhibited scalers; scalers are computer-readable counting devices. The inhibited scalar counts only while the data acquisition system (DAQ) is live and accepting new data. The uninhibited scaler counts continuously. A comparison of the two scalers provides a measurement of the dead time of the system.

A time-to-digital converter (TDC) is an electronic module that measures the time difference between an input start signal and an input stop signal. The start signal is derived from a signal provided by the HIGS accelerator indicating the arrival of a "bunch" of photons. The photons from the accelerator travel in bunches that are 180 ns apart; the accelerator will be further discussed in section 2.3.1. The stop signal is the output logic pulse from the

discriminator connected to each detector cell.

The TDC output can be calibrated to obtain the time-of-flight (ToF) of a particle from the target to the *Blowfish* cell. Since photons that are Compton scattered from the target travel at the speed of light and neutrons from the target travel much slower, the ToF provides a means for these two event types to be separated [Wur10].

Trigger Logic

A trigger is a signal that alerts the data acquisition system (DAQ) that it must read data from the ADCs and TDCs. In a normal experimental run there are a number of different conditions that can cause a trigger. The set of triggers are the neutron, pedestal, flasher and gain monitoring triggers. The flasher and gain monitoring triggers will be discussed in chapter 3; these are present during the gain calibration. Any trigger will also set a data latch. The data latch prevents further signals from reaching the the ADC and TDC modules until the DAQ has finished reading out the modules. The data latch also inhibits the scalers from counting since the DAQ is not "live" during this time. The DAQ software resets the data latch when module readout is complete.

The neutron trigger occurs when the *Blowfish* neutron detectors detect a particle; it is set by a logic OR of all the neutron detector cells. However not all cell signals are allowed to contribute to the neutron trigger. For most events a veto on the neutron trigger is applied during the time that Compton scattered gamma rays from the target are expected to arrive at the detector cells. The neutron trigger also generates the gates to the ADCs recording the pulses from each detector cell.

The pedestal trigger measures the offsets that are present in the output of each ADC module. This offset is present because a small continuous amount of charge is injected into the ADC circuit in order for the module to perform linearly. Normally the ADC does not provide an output unless the signal is above a predefined minimum value. During the pedestal trigger the module is instructed by the DAQ software to not apply this suppression. Then the ADC provides an output even when there is no input signal. This allows the offset, or pedestal as it is known, to me measured. The pedestal trigger works collectively with the neutron trigger; and it also has a veto that insures that the pedestal trigger only occurs
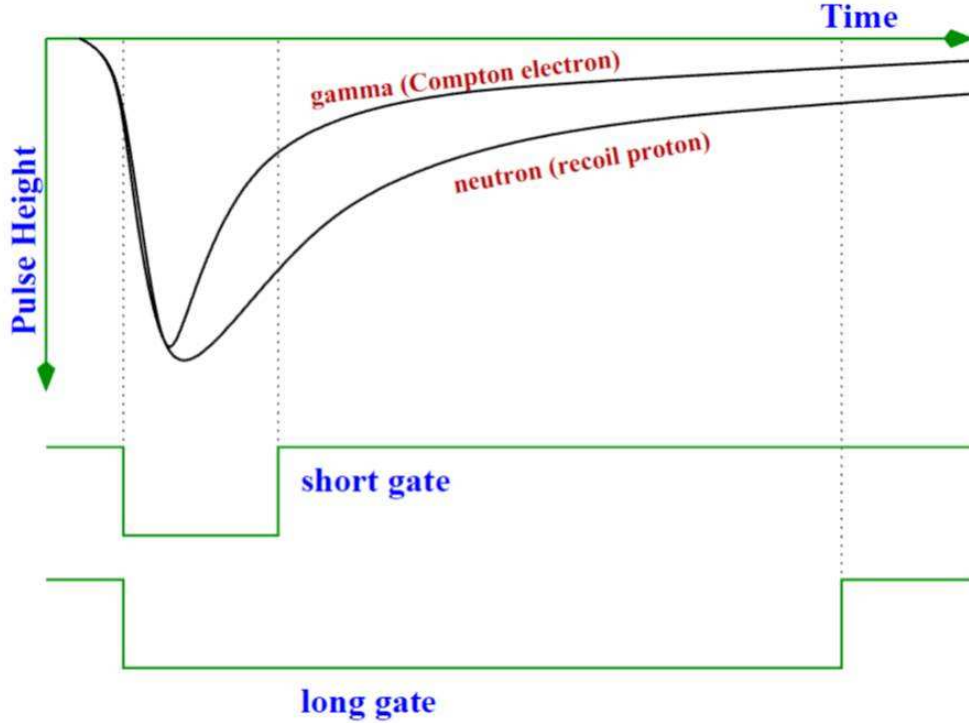
Figure 2.7: The PSD parameter is the difference of the scintillator differential light output integrated with a long and short gate. The upper two lines are typical differential light output curves for BC-505; the bottom two digital signals represent the long and short gates used in the integration (image credit: [Saw05]).

during the time window that a neutron could be present [Wur10].

2.2.2 Pulse Shaped Discrimination: PSD

Pulse shaped discrimination, PSD, is the method of distinguishing between different types of incident particles by examining the shape of the light pulses from scintillation detectors. Neutrons and photons are both neutral particles and need to interact with charged particles in order to produce a detectable signal. Photons are measured by the processes described in section 2.1.4 and neutrons are measured by the process discussed in section 2.1.5. The result is that photons produce a detector output pulse that is shorter than the output pulse when neutrons hit the detector. Figure 2.7 depicts these output pulses [Kuc10].

As mentioned in section 2.2.1 the analogue signal from each cell is split into two ADCs; one with a short gate and one with a long gate. These gates are also shown in figure 2.7. An ADC only integrates the input current pulse during the time the gate is active (negative).

Since the photon pulse is shorter, a larger fraction of its signal will appear in the short-gated ADC than for a neutron pulse. This provides a means by which photon and neutron pulses can be separated. If the ADC value from the long-gated ADC is L, and the ADC value from the short-gated ADC is S, a PSD parameter can be defined by

$$PSD = \frac{L - S}{L}. \tag{2.7}$$

Large values of this PSD parameter correspond to neutron while smaller values correspond to photons. Using a radioactive source that produces both neutron and gamma-rays the PSD parameter can be calibrated to provide good separation of neutrons and gamma-rays for signals above a given light output threshold.

2.3 Experimental Set Up

The general layout of the experimental components for the proposed GDH measurement at the HIGS facility is depicted in Figure 2.8. The various components will be described in the following sections.

2.3.1 High Intensity Gamma Source

The High Intensity Gamma Source (HIGS) is a part of the DFEL (Duke Free Electron Laser) Laboratory; which is managed by the Triangle Universities Nuclear Laboratory (TUNL). These facilities are located at Duke University campus in Durham, North Carolina, USA. Figure 2.9 shows the layout of the DFEL facility.

The HIGS uses a free electron laser that has the ability to produce entirely linear or circularly polarized photons in the range of 2-100 MeV with a gamma-ray flux between 10^7 and 10^9 photons [LBE$^+$97]. The operating principle at HIGS is the Compton backscattering of the free-electron laser photons from electrons in the storage ring.

A 280 MeV linear accelerator, also known as a *linac*, is used to inject electron bunches into a booster ring; where they are accelerated to energies up to 1.2 GeV; then the electron bunches are fed to the storage ring [WAG$^+$09].

Legend:
- Vacuum
- Gamma Ray
- Collimator
- 5 Paddle Flux monitor
- Target Cooling System
- Target
- *Blowfish* Detector
- NaI Crystal

upstream target room   Main Gamma-Vault (downstream)   *Not to scale*
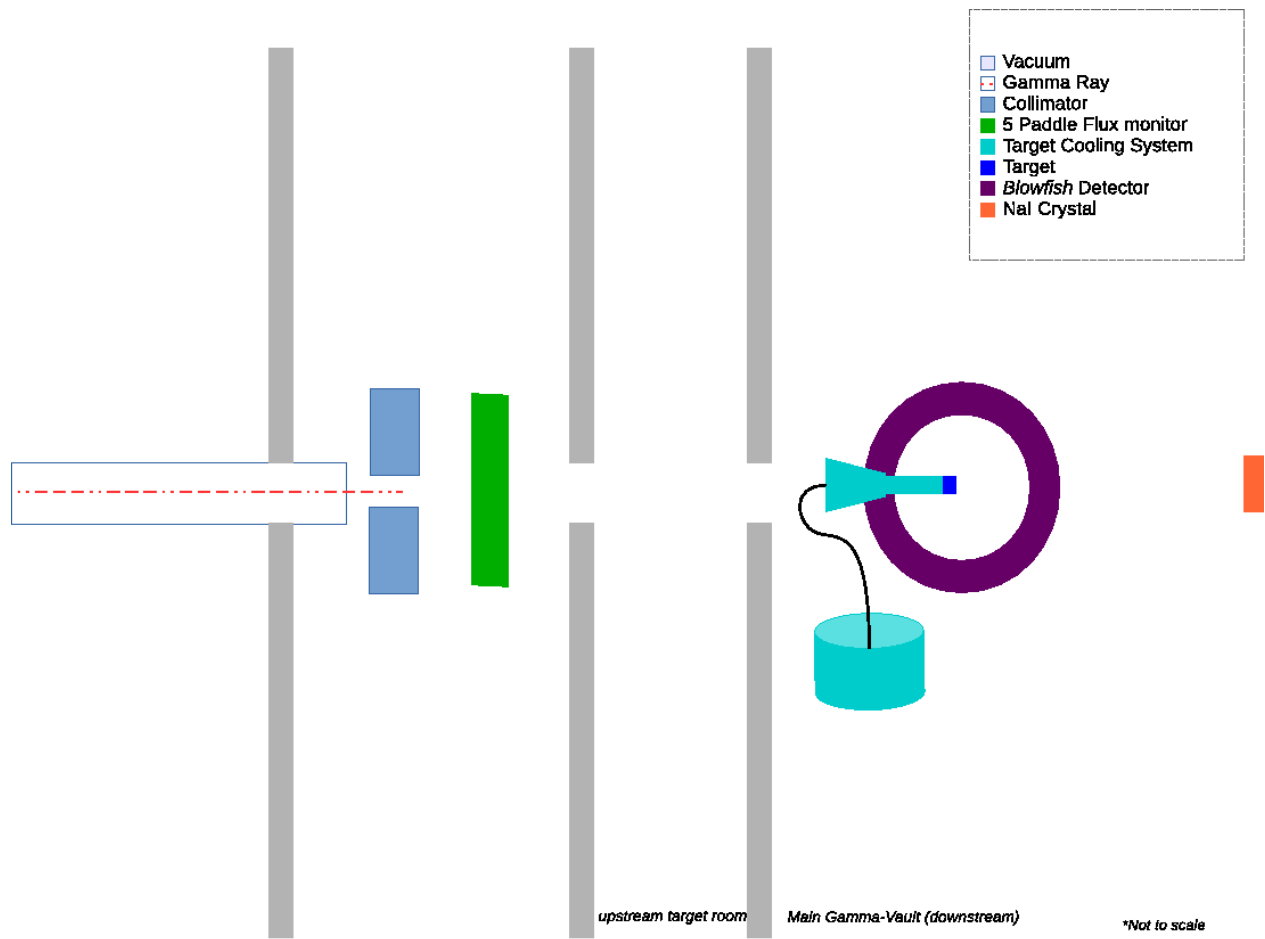
Figure 2.8: Top view, not to scale, of the experimental layout for the up coming GDH experiment
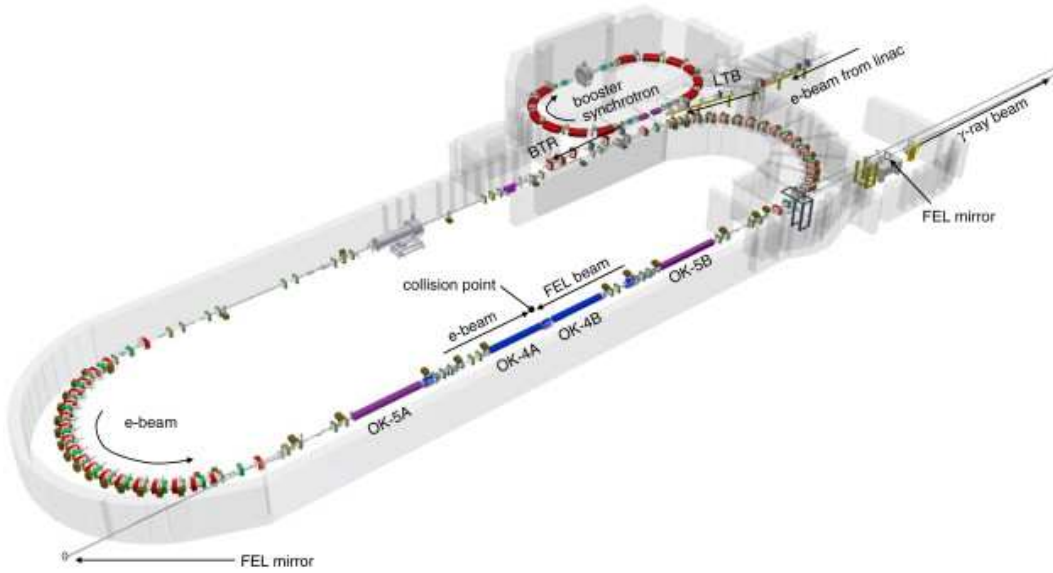
Figure 2.9: The HIGS facility layout for the Free-Electron Laser (image courtesy of the HIGS facility).

Within the storage ring, ultraviolet (UV) radiation is produced by the an electron bunch travelling through a set of undulators, a region of rapidly alternating magnetic fields. The formal nomenclature is Optical Klystrons (OK); where the OK-5A/B helically polarize, and the OK-4A/B facilitate the linear polarization. Once the electron bunch circulates around the storage ring, the UV photons reflect off of both mirrors and are in sync with the electrons; this causes additional UV photons to be radiated in the undulators. High energy photons, gamma rays, are produced when a second bunch of electrons are injected into the storage ring at the moment the first electron bunch is half way through the storage ring; so the second electron bunch meets the UV photons, travelling in the opposite direction, right in the middle of the optical cavity. Backscattering occurs when the UV photon collides with the second bunch of electrons, resulting in a high energy photon. This final product, a gamma-ray with a set energy and polarization, travels through the UV mirror to the downstream target rooms; where the beam will collide with an experiment target. The FEL laser light has a wavelength that is set by the FEL mirrors, and ranges from infrared to UV. The resulting gamma-ray energy can be changed by varying the electron beam energy in the storage ring [WAG+09].

Compton Backscattering

The backward scattering of UV photons against high-energy electron bunches is the method used at the HIGS facility to create a high flux, polarized, gamma ray beam.

The Compton backscattering technique is well established in several laboratories, and provides highly polarized photon beams of good energy resolution and very low background. The advantage of the FEL technique is that it enables the production of very high fluxes with tunable energies [WAG+09].

The general kinematic description of the Compton backscattering technique is the direct collision of the relativistic electrons and photons. As described in Leitvinenko et al.'s paper on the Gamma-Ray Production in a Storage Ring Free-Electron Laser [LBE+97] the Compton backscattering is used to create a 'pencil-like' beam of γ-rays with energy E_γ. For the case of $\gamma = E_e/m_e c^2 >> 1$, the energy of the γ-ray beam is,

$$E_{gamma} = \frac{4\gamma^2 E_{ph}}{1 + (\gamma\theta^2) + 4\gamma\frac{E_\gamma}{m_e c^2}}, \tag{2.8}$$

where E_{ph} is the energy of the initial FEL photons; θ is the angle between the direction of the incident electrons and the generated γ-ray beam; the energy of the incident electrons is given by E_e. The energy of the gamma-ray beam depends strongly on the angle θ; the peak of E_γ occurs when $\theta = 0$; A collimator may be used to restrict the range of angles θ that will be incident on the target, therefore setting the energy resolution of the γ-ray beam [LBE+97].

2.3.2   Target

HIFROST

The target that will be used for the GDH experiment is the HIGS Frozen Spin Polarized Target, the abridged name is HIFROST. HIFROST is a nuclear polarized target system developed by our collaborators at the University of Virginia and the HIGS facility. The HIFROST system is designed for making measurements of single-polarized and double-polarized observable reactions. The target system is comprised of a cooling component, the refrigerator, a holding coil, to contain the supercooled target; a NMR system, is a Liverpool Q-meter; and a microwave generator.

Figure 2.10: Picture of the HIFROST target's cooling system in its first cool down test in September 2013

In order to polarize a solid target, consisting of either chemically doped beads or irradiated beads, is refrigerated to a temperature at a fraction of a Kelvin (just above absolute zero). The target will be hydrogen rich, and composed of deuterium,^{2}H.

The supercooled target temperature is maintained by the refrigerator system, as seen in figure 2.10. The refrigerator is built around the target, and set up to be parallel to the beam.

The mixing chamber is a key component of the refrigerator; it's a vessel that cools a mixture of ^{3}He / ^{4}He isotopes below liquid evaporative temperatures. The chamber utilizes a process called dilution to bring the mixing chamber temperature to under 1 K. Dilution utilizes the endothermic reaction associated with the two phases of the helium mixtures.

Nuclear Magnetic Resonance (NMR), a process in which resonance variations are detected by observing the radio frequency power absorbed at resonance, is used to measure the polarization of the target [Kra88]. In HIFROST, the system that measures the polarization is the Liverpool NMR Module; the module consists of a Q-Meter, which contains the capacitor and resistor for the LCR circuit. A LCR circuit is comprised of a resistor, inductor, and a

capacitor; then the inductor of this circuit is a coil located near the target. This inductance changes as a function of the magnetic sensitivity of the nuclei. Since the magnetic sensitivity and polarization are related, the resonance of the LCR circuit will give us information to find the polarization of the target material. Knowing the polarization of the target is an essential component in the GDH experiment. Figure 2.6 shows a simulation of *Blowfish* with with HIFROST.

D_2O Target

For deuteron photodisintegration measurements that do to use a polarized target, a D_2O (heavy water) target is used. The D_2O is held in a Lucite cylindrical container which is suspended in the centre of *Blowfish*. This is shown in figure 2.15.

2.3.3   Five-Paddle Flux Monitor

A flux monitor is used to measure the number of gamma-rays incident on the target. The five-paddle flux monitor was constructed by Octavian Mavrichi, under the supervision of Dr. Rob Pywell, for Mavrichi's Master's thesis project [Mav10]. This was an upgrade on the three-paddle and one-paddle flux monitor; and the upgraded five-paddle has the capability of measuring the HIGS beam flux within a systematic uncertainty of 2%. See Figure 2.11 for an image of the five-paddle flux monitor.

The five-paddle flux monitor is comprised of five scintillator paddles. Each paddle is comprised of a ~ 2 mm thick piece of solid plastic organic scintillator, BC-400; this is joined to a light guide. The light guide is a solid trapezoidal piece that is adhered to a cylindrical piece; all of which are wrapped in a reflective foil wrapper. The light guide is adhered to the BC-400 scintillator by a transparent adhesive. Then the cylindrical part of the light guide is connected to the PMT through a silicone "cookie", that provides optical coupling between the light guide and the PMT. The entire paddle and PMT is made light-tight, so that no external light interacts with the scintillator, via the reflective foil wrapping and black plastic tape.

The five paddles are held in place by a custom made aluminum frame. Two paddles are upstream of a 2 mm aluminum converter and three paddles are downstream from the
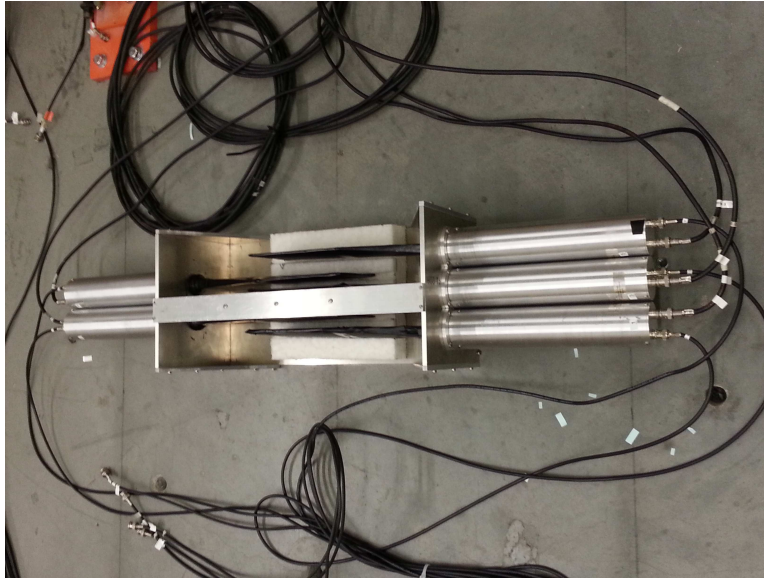
Figure 2.11: The five-paddle flux monitor being tested after repairs in September 2013.

converter; all are placed approximately equidistant from each other. The aluminum converter produces electrons and positrons when hit by the incoming gamma ray photons, via Compton scattering or pair production. [PMWW09, Mav10].

During the September 2013 visit to the HIGS facility, the flux monitor was taken apart and reassembled because it had suffered an external trauma. Figure 2.11 show a picture of the flux monitor undergoing tests after reassembly.

Figure 2.12 illustrates the gamma-ray beam's interaction with the five-paddle flux monitor. The recoiling electrons and positrons, from the converter, deposit a small amount of energy in each of the downstream paddles as they pass through the paddles.

An output pulse from the flux monitor is defined by a triple coincidence between the three downstream paddles in anti-coincidence with the second (veto) paddle. The anti-coincidence prevents charged particles coming along with the gamma-ray beam, or cosmic rays, from triggering the flux monitor. The triple coincidence requirement ensures that the detected event is only due to the recoiling electron or positrons; signals from radioactivity in the room are effectively rejected.

The efficiency of the flux monitor, for detecting photons, is deliberately chosen to be low. Therefore, most of the photon beam passes through to the experiment target.
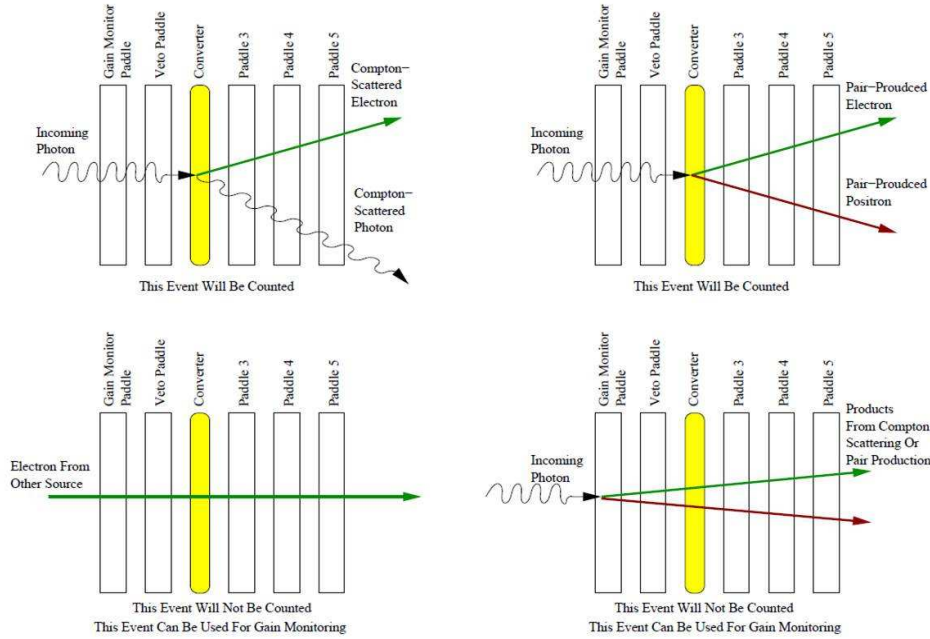
Figure 2.12: Image of how the five-paddle flux monitoring system's triple coincidence operates (image credit: W.Wurtz [Wur10]).

The efficiency of the flux monitor is determined by inter-calibrating with a sodium iodide (NaI) photon detector, which is placed down stream of the flux monitor. The NaI detector is 100% efficient, for detecting the gamma-ray energies used in our experiments. Using the flux monitor we can determine the number of incident photons on the experiment's target, which is necessary for extracting the absolute cross sections.

2.3.4   Software Tools

Several pieces of software are used for data acquisition and analysis of our experimental data.

Data Acquisition: LUCID

LUCID [DM95] is the software system that was created to control the data acquisition process and to preform basic analysis on the data as it is acquired. The major components of the LUCID system are illustrated in figure 2.13.

LUCID is comprised of three major software components: the Reader, Writer, and Looker. The major part of the Reader software resides in a front-end computer running the RTEMS
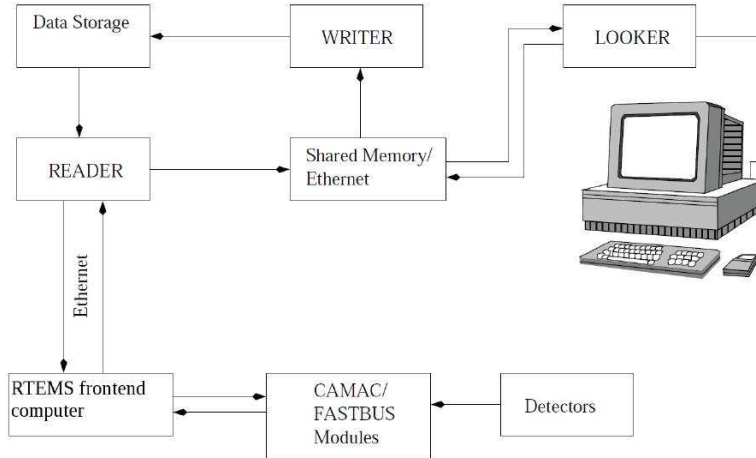
Figure 2.13: Formalistic summary of the data acquisition system illustrating the connection between Blowfish and Lucid (image credit: [Saw05]).

real-time operating system [Cha08]. The front-end computer interfaces with the VME and CAMAC hardware containing the data acquisition modules. The software running on the front-end computer responds to triggers (see section 2.2.1) and reads the data from the modules. The data is then transferred, via ethernet, to the main computer controlling the acquisition, where the data is put into a shared memory buffer. The Writer part of the LUCID system then transfers the data to a data storage device. While the data resides in the shared memory, the Looker part of the LUCID software can do some preliminary analysis and build histograms for the user to monitor the progress of data taking. The functions performed by the Reader, Looker and Writer can be defined by the user in simple description files. The data taking by LUCID can be controlled and monitored by a visual interface (known as GXLUCID) which runs on the main data acquisition computer. Previously recorded data may also be analyzed by the Looker software. In that case the Reader software simply reads data from a data storage device.

Lucid is ideal for data acquisition due to the simplicity of its structure for the user. However, the final data analysis is done using the ROOT data analysis framework.

Data Analysis: ROOT

ROOT is an analysis program that provides the groundwork for data processing; it was created at CERN (the European Council for Nuclear Research). It is integral to the area
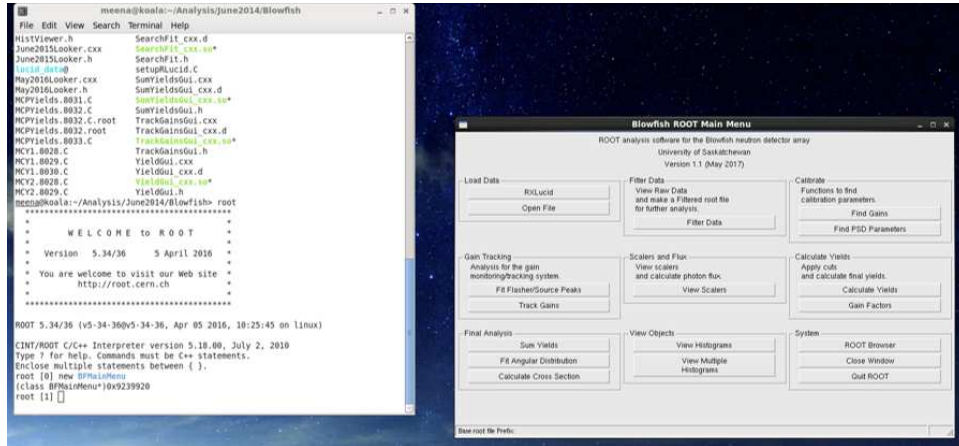
Figure 2.14: The BFRoot main menu

of high-energy physics research [BR97]. ROOT provides a data analysis package that is capable of dealing with large data files, statistical analysis, visualization and storage. ROOT's structural programming easily integrates with various coding languages; and has made it easy to create additional analysis packages, which provide for specialized treatment of the data.

For the analysis of data for his thesis, Ward Wurtz [Wur10] created a specialized analysis package that provided a more efficient way to calibrate and analyze data obtained by the *Blowfish* detector; it is referred to as the Blowfish-ROOT analysis package, BFRoot being the shortened name.

As a first step in the analysis of our data with ROOT, the data must first be converted from the format written by the LUCID system into a more compact ROOT file. This is accomplished by a package known as RLucid [WP16].

BFROOT

The Blowfish-ROOT (BFRoot) analysis package was initially written by Wurtz [Wur10]. Wurtz's initial code was the partial structure for Rob Pywell's May 2017 update [Pyw17]. As before, BFRoot contains C++ codes that run within the ROOT environment. The majority of BFRoot's functionality can be controlled through a visual interface that simplifies the analysis tasks. The graphical interface to BFRoot may be started by executing "`new BFMainMenu`" at a ROOT prompt. This is shown in Figure 2.14.

The following steps were taken to analyze the data pertaining to this thesis. Initially the

data needs to be loaded; if the format of the data was already in ROOT format then the **Open File** function was used; and if the format of the data was in Lucid format then the **RXLucid** function was used to convert the Lucid data file to a ROOT data file, using the RLucid program.

Once the data file was opened; the raw data was filtered using the **Filter Data** function. This action cuts out events where more than one one of the *Blowfish* cells had a hit. This is done because, for multiple hits, the timing of the ADC long and short gates may not be correct, and therefore such events will not have good PSD. While making the multiplicity cuts, you're able to view the raw digitized data; this is a way to determine how well the individual *Blowfish* cells are functioning. The filtering also corrects the ADC values for pedestals (see section 2.2.1) and provides a way to check that the pedestals are correct.

The next step was to calibrate the data by finding the gains from data runs where a radioactive source of known energy gamma rays was placed in *Blowfish*. The gains were calculated and saved by utilizing the **Find Gains** graphic interface. This function builds histograms of the ADC output for all 88 cells, which are then fitted to find the ADC value of the Compton edge. This knowing the gamma-ray energy of the source used, the gain for each cell may be calculated. The fitting process is describe more fully in chapter 3.

As mentioned previously, the gain of each cell may change with time. Chapter 3 will describe a system that allows the gain to be tracked during a data taking run by using an LED light pulser system know as "Flashers". The analysis of events associated with this gain tracking system may be done using functions under the Gain Tracking heading. The **Fit Flasher/ Source Peaks** function finds information from events when the LED light pulser fires. The **Track Gains** function takes information from gain tracking system and uses the gains found from source calibration runs to calculate the gain for each cell for each individual run. The results of experiments designed to test this system will be presented in chapter 4.

BFRoot provides many other functions necessary for the full analysis of experimental data. We have mentioned above only those functions that are central to the analysis performed in this thesis.

Detector Simulation: GEANT4

Simulations of the the neutron detector *Blowfish* and the five-paddle flux monitor, are critical to understanding these systems. The simulations were built using the GEANT4 toolkit [AAA+03, AAA+06, AAA+16], in C++ code. **GEANT4** is a toolkit for the simulation of the passage of particles through matter. **GEANT** stands for **Ge**ometry **An**d **T**racking. Its application fields include high energy, nuclear and accelerator physics, as well as studies in medical and space physics. These functions are based on primary logic, or from previously defined libraries that contain the fundamental properties of materials, particles and interactions between them.

The simulation takes into account the physical layout of the detector system, the size and shape of the incident gamma-ray beam, the target geometry and the resolution of the active detector cells. These factors are dependent on one another when finding the absolute cross sections and other quantities of concern. Since we are not able to directly determine the effect these factors have on the data, we are unable to carry out a deconvolution (in the experimental sense) and calculate the desired quantities. So to overcome these combined factors we utilize, the comprehensive Monte-Carlo simulation, to preform the deconvolution [Wur10].

GEANT4 outfits us with the tools to solve the convolution problems. The simulation for the GDH experiment includes the cryogenic target, the *Blowfish* array and its support structure. A GEANT4 rendering of the experimental setup is shown in figure 2.15.

Our simulation of *Blowfish* has undergone many iterations. A version known as *BlowfishX* was designed by W.A. Wurtz for his dissertation [Wur10]; this was based on earlier work by R. Pywell. Since then the simulation has been largely rewritten because there were major changes needed to accommodate the GDH target. As well the code describing the geometry of the individual cells has been much improved, including recent changes to the mounting system of the cells. The simulation's data output is in LUCID format, just the same as for a real experiment. This allows the same analysis software to be used on both sets of data.

A simulation *run* consists of a predefined number of *events*. A event begins with the generation of a particle; in our case a neutron. The initial location of the neutron is chosen
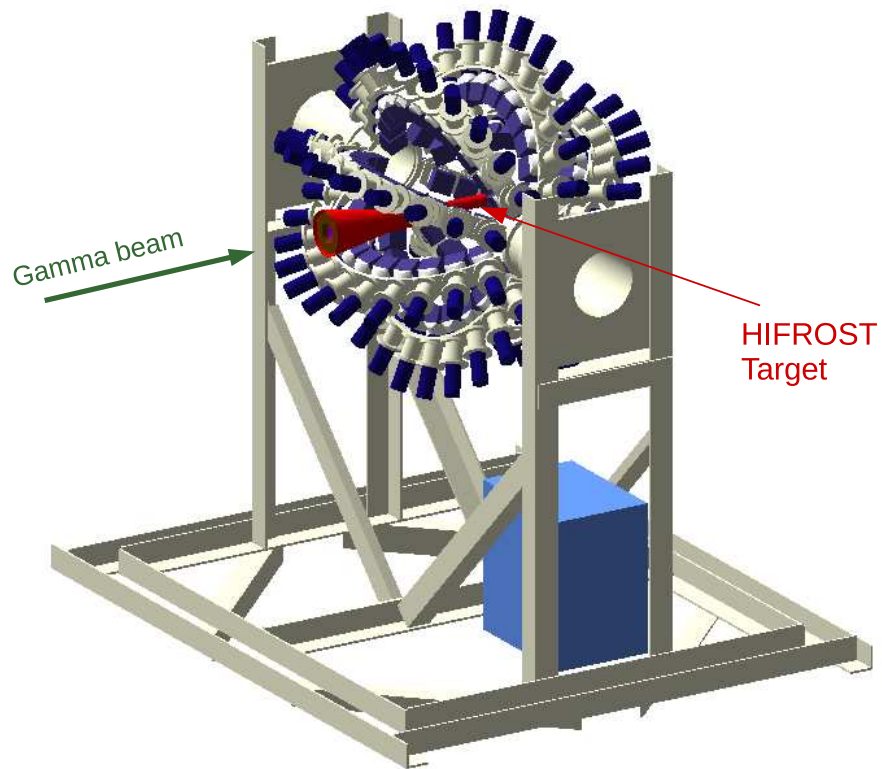
Figure 2.15: The updated GEANT4 simulation of Blowfish in the GDH orientation (image courtesy of Rob Pywell).

randomly within the target and taking into account the gamma-ray beam size and its intensity at each point within the target. The momentum of the neutron is determined from the kinematics of the reaction under study. The distribution of the outgoing neutron's direction and energy can be calculated using an assumed differential cross section for the reaction.

The neutron is then tracked through all the materials defined in the simulation. At each step in the tracking, the probability that the neutron undergoes an interaction with the material is determined, and whether or not an interaction does occur is chosen randomly according to that probability. All possible interactions are simulated, including scattering and nuclear reactions. If additional particles are created in an interaction they are also tracked. Tracking continues until all particles come to rest or pass outside the "world" defined by the simulation.

If any particle passes through materials in the simulation that are defined to be detectors, such as the BC-505 in the *Blowfish* detector cells, any energy deposited in that material is recorded. The light output, resulting from this energy deposited, is calculated according the function described in section 2.1.3. The time, from the start of the event, when energy is deposited in a detector is also recorded.

At the end of an event, when all particles have come to rest, the light output in each detector cell is converted to ADC output values using an assumed gain for that detector. The time when energy is deposited is converted to a TDC value. These ADC and TDC values are recorded in the output data file and another *event* is initiated.

The output of a simulation is analyzed in the same way as for real data using the same analysis cuts. In particular, the analysis of simulated data uses the same light output threshold cut that was used for real data. A comparison between the number of neutrons detected in the simulation and in the real data allows the efficiency, and hence the cross section for the reaction to be determined. In the analysis of the simulation data the light output threshold is known exactly since it is set in the simulation. In the analysis of the real data, however, the application of the light output threshold assumes that the gain in the experiment is known accurately.

The determination of the gain is the subject of the next chapter.

CHAPTER 3

GAIN

Our definition of the gain is,

$$\text{gain} \equiv \frac{\text{Light Output}}{\text{ADC Output}}.$$

For *Blowfish* and our experimental set-up, it is important to be able to determine the gain and to determine whether any changes in the gain can be tracked throughout the course of a day.

3.1   Gain Calibration

The gain calibration is done by placing a radioactive source at approximately the centre of *Blowfish*; for the measurements described in this thesis the radioactive source used was Cesium 137, a gamma source.

As the radioactive source's gamma-rays enter the detectors, Compton scattering results in a recoil electron, which causes scintillation as the recoil electron deposits energy. The maximum energy of a recoil electron occurs when the incoming photon scatters at 180° with respect to the initial photon direction; this creates what is known as the Compton edge. This process can be repeated by the scattered photon if it has enough energy. The repeated process can lead to an energy deposited greater than the Compton edge. The energy of the gamma rays from the radioactive source is known. The energy of the initial photon is E_γ. If the photon scatters at an angle θ with respect to the initial photon's direction, the energy of the scattered photon is E'_γ. The relation between these energies is given by

$$\frac{1}{E'_\gamma} - \frac{1}{E_\gamma} = \frac{1}{m_o c^2}(1 - cos\theta), \tag{3.1}$$

36
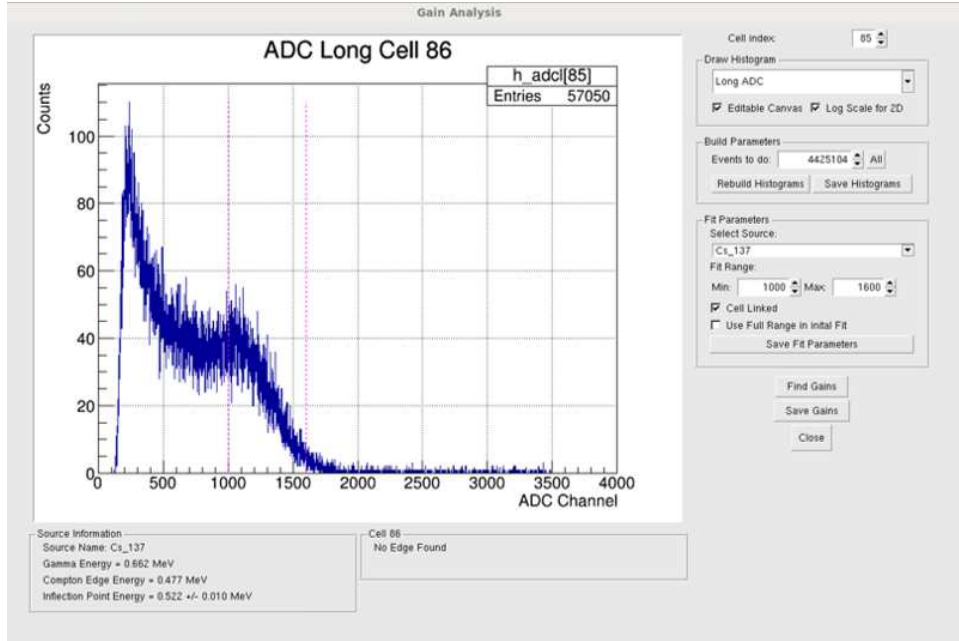
Figure 3.1: The light output spectrum when a Cesium-137 source is used for *Blowfish*'s cell 86. This is taken from run 1561 (see table 4.1).

where $m_o c^2$ is the rest energy of an electron. Refer to figure 2.4 for a depiction of the Compton scattering effect. The Compton edge occurs when $\theta = 180°$. The Compton edge energy, E_C, which is the maximum energy of the recoil electron, is,

$$E_C = \frac{2E_\gamma^2}{m_o c^2 + 2E_\gamma}. \tag{3.2}$$

If the Compton edge appears at channel A_i for *Blowfish* cell i, the the gain of that cell is

$$g_i = \frac{E_C}{A_i}. \tag{3.3}$$

The Compton edge is located by fitting a curve to the end point of the light output spectrum. An example of a light output spectrum when a ^{137}Cs source is used is shown in figure 3.1.

The function used to fit to the data is modelled as one side of a Gaussian with a linear background. Since the Compton edge in the light output spectrum is likely to have a sharp edge convoluted with the detector resolution; the fitting function provides a more realistic shape for the endpoint. The fitting function is given by,

$$f(x) = a_0 + a_1 x + a_2 e^{-\frac{(x-a_3)^2}{2a_4^2}}. \tag{3.4}$$
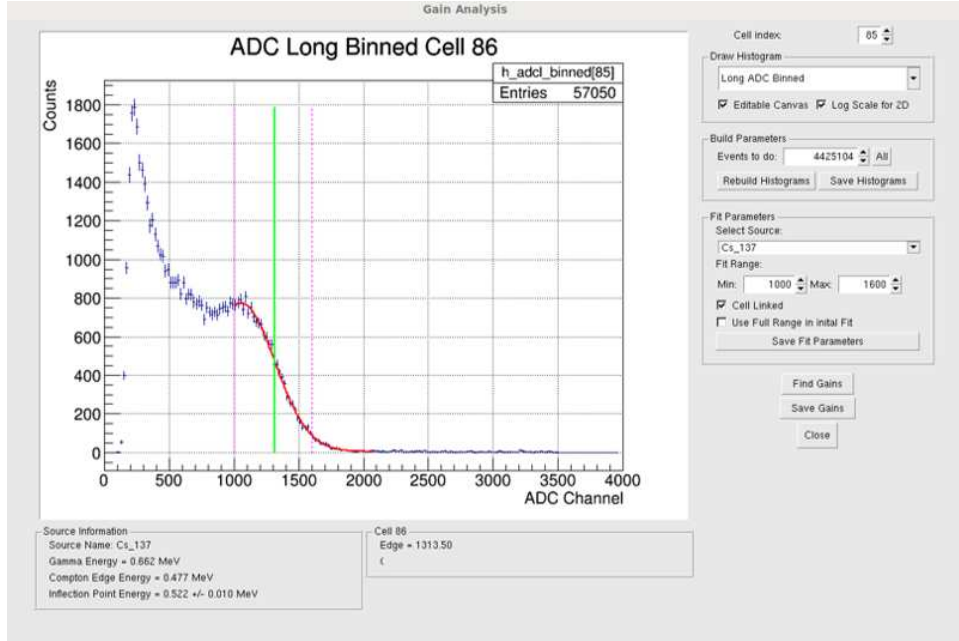
Figure 3.2: The binned version of the light output spectrum for Cesium-137 for cell 86. This is taken from run 1561 (see table 4.1).

The inflection point of a Gaussian is at one standard deviation from the midpoint of a Gaussian; so the inflection point is found using the following equation,

$$E_{InflectionPoint} = a_3 + a_4. \tag{3.5}$$

The fitting algorithm first re-bins the raw data into a histogram with bin widths of 20 ADC channels; figure 3.2 is an example of the light output spectrum binned for *Blowfish* cell 86 for run 1561 (see table 4.1). Next, an initial guess for the $E_{InflectionPoint}$ is found from the position with the maximum negative slope, in this re-binned histogram. This provides initial guesses for a_3 and a_4 . After the initial fit, a second fit is done with a restricted fit range (determined by the initial fit) from $a_3 - 0.15a_4$ to $a_3 + 3a_4$.

The GEANT simulation of *Blowfish* is used to determine the relationship between the inflection point and the actual Compton edge. In the *Blowfish* simulation, gamma rays of a monochromatic energy are released from the centre of the *Blowfish* detector; and light output spectra are recorded for the *Blowfish* cells. Using a range of photon energies, the simulation is used to find a function relating the inflection point to the Compton edge energy. A best

38
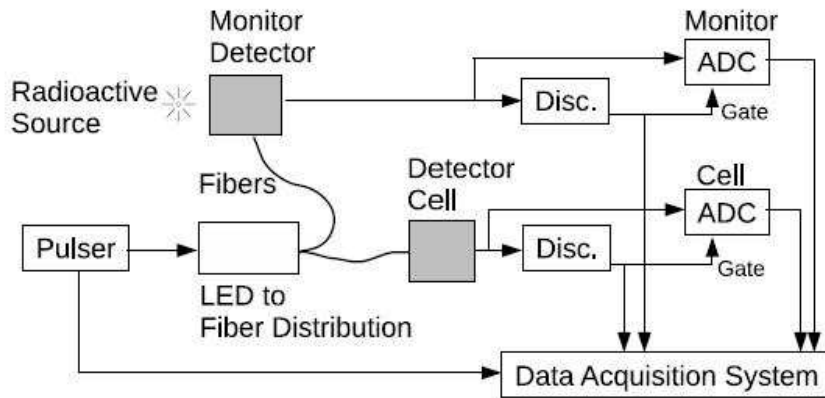
Figure 3.3: Conceptual schematic of the gain monitoring system (image credit: [BPIW09])

fit is found with the function,

$$\Delta E_C = 0.100 - \frac{0.038}{\sqrt{E_C}} \text{ MeV}. \tag{3.6}$$

This takes into account the energy dependence of the resolution of the detector cells.

Figure 3.2 shows an example of the fit to the Compton edge. If A_i is the ADC channel number of the fitted inflection point; and a gamma source with the Compton edge energy of E_C is placed near *Blowfish*; Then the gain for cell i is calculated by,

$$g_i = \frac{(E_C + \Delta E_C)}{A_i}. \tag{3.7}$$

The gains for each of the *Blowfish* cells are all determined using this method.

3.2   Gain Monitoring System

The gain monitoring system tracks the gains of *Blowfish*'s detectors; the system was designed and installed by Brian Bewer [Bew05]. This system was designed to monitor the gains by using flashes of light from continuously calibrated Light Emitting Diodes (LED). This system of LEDs has been named the Flasher System. Figure 3.3 provides a schematic of the gain monitoring system.

3.2.1 Flasher System

Four LEDs are contained in lightproof metal boxes, mounted to *Blowfish*; and each LED is connected to a bundle of 30 fibre optic cables. 22 of the fibres are connected to 22 of the *Blowfish* cells. The flashers are driven by a pulser, a square pulse generator, which is regulated by the DAQ system. If the light pulse delivered by the LEDs is constant in amplitude, the signal recorded from the cell when the flasher fires should be at a constant ADC channel if the gain of the cell is constant. Variations in the flasher ADC channel would indicate a change in the gain.

To account for possible variations in the LED intensity the flashers have their own monitoring system. One of the fibre optic cables from each of four LED boxes connects a gadolinium-silicon-trioxide (GSO) inorganic scintillator. The GSO scintillators are used to continuously measure the LED light output in order to detect any drifting of the LED intensity. In order to make sure the GSO detectors themselves aren't drifting a radioactive source is placed near the 4 GSO scintillators so that they can be continuously monitored for their own gain.

Gain Monitor Trigger System

The trigger logic for the gain monitoring system consist of monitor trigger and a flasher trigger.

The gain monitoring system is connected to the same data acquisition (DAQ) system as the neutron detector electronics. Periodically throughout an experiment a trigger from the GSO monitor detectors is enabled. This allows recording of a signal from the radioactive source near the GSO monitor to track the gain of this monitor. The trigger that prompts the DAQ to read out the ADC connected to the GSO monitor detectors is known as a monitor trigger.

Also periodically throughout an experiment a light flash is enabled from the LEDs by the DAQ system. The resulting light flash generates signals from all of the *Blowfish* cells and from the GSO monitor detectors. These signals generate a trigger, known as a flasher trigger, that prompts the DAQ to read the ADC for all the *Blowfish* cells and the GSO

monitor detectors.

3.2.2 Gain Tracking Principles

If an amount of light L is produced by the LED, and a certain fraction x_i of it reaches cell i, then the peak due to the LED flasher will appear in channel

$$A_{Fi} = \frac{x_i L}{g_i},$$
(3.8)

where g_i is the gain of cell i [BPIW09]. If a feature from the radioactive source near the monitor detector m with light output E_M is observed to be at ADC channel A_m then the gain of the monitor detector m is determined by,

$$g_m = \frac{E_M}{A_m}.$$
(3.9)

If the fraction of the LED light L reaching the monitor detector is x_m, then the peak due to the LED flasher in the monitor histogram will appear in channel,

$$A_{Fm} = \frac{x_m L}{g_m}.$$
(3.10)

All the quantities here are known or measured except L, x_i, and x_m. Combining equations (3.8) and (3.10) the ratio for each cell, R_i can be calculated using,

$$R_i = \frac{x_i}{x_m} = \frac{g_i}{g_m} \frac{A_{Fi}}{A_{Fm}}.$$
(3.11)

The light produced by the LED L, the gains of the cells g_i, and the gain of the monitor detectors g_m may be subject to change as the data is obtained; the changed quantities are, respectively, denoted by L', g_i', and g_m'. Then if the source feature in the monitor spectrum appears at channel A_m' the gain of the monitor detector is now

$$g_m' = \frac{E_M}{A_m'}.$$
(3.12)

We allow the fraction of the LED light reaching cell i to now be x_i' and the fraction of the LED light reaching the monitor detector m to now be x_m'. Then the flasher peak will appear in the cell spectrum at channel,

$$A'_{Fi} = \frac{x_i' L'}{g_i'}.$$
(3.13)

41

Additionally the flasher peak in the monitor detector spectrum is at channel

$$A'_{Fm} = \frac{x'_m L'}{g'_m}.$$

(3.14)

Combining equations (3.13) and (3.14) the cell gain becomes,

$$g'_i = g'_m \frac{A'_{Fm}}{A_{Fi}} \frac{x'_i}{x'_m}$$
$$= g'_m \frac{A'_{Fm}}{A'_{Fi}} R'_i,$$

(3.15)

where $R'_i = \frac{x'_i}{x'_m}$.

The gain tracking system relies on being able to make the assumption that $R'_i = R_i$; the ratio should not change throughout the day. This assumption is legitimate as long as there are no mechanical changes between the two runs that could change the light transport efficiency along the fibres, i.e. a change in x_i or x_m. The required cell gain in the data taking run is then [BPIW09],

$$g'_i = g'_m R_i \frac{A'_{Fm}}{A'_{Fi}}.$$

(3.16)

The R-value, R_i, can be measured in a calibration run with a radioactive source. In a later data taking run, without the source in place, the values g'_m, A'_{Fm}, and A'_{Fi} can be measured using the flasher and monitor event data. The the gain g'_i for each cell i in the data taking run can be calculated.

3.3   Experimental Impact of the Gain

As previously mentioned, the efficiency of the detector depends on the light output threshold, the lower level integration limit of the light output curve (refer to figure 1.3). This in turn depends on the knowledge of the gain of the detector. Therefore an uncertainty in the gain translates into an uncertainty in the detector efficiency.

Since we know that the gain of a detector can change, during an experiment the gain is determined using a radioactive source at least once in each day of data taking. At other times we assume we can track the gain using the gain monitoring system. As mentioned above, this relies on the assumption that $R'_i = R_i$ throughout the time between when gain calibrations

with a radioactive source are performed. This is the assumption that is scrutinized by a series of measurements that will be described in the next chapter.

There are three major questions that will be addressed with these measurements.

- The stability of the gain of each *Blowfish* cell as a function of time.

- The validity of the assumption that $R_i' = R_i$.

- How well the gain predicted by equation (3.16), using the LED flasher gain monitoring system, is related to the true gain.

The concluding part of the next chapter will use a simulation to establish the impact that an uncertainty in the gain has on the uncertainty in a calculated cross section.

CHAPTER 4

RESULTS

4.1 Data

The data collected during the July 2014 visit to the HIGS facility were from a series of calibration runs. The calibration runs consist of a radioactive source placed approximately near the centre of the *Blowfish* detector.

The two sources used were Cesium-137, ^{137}Cs, and Americium-Beryllium, AmBe. The ^{137}Cs has a relatively long half life and its gamma ray spectrum is well established and relatively simple. It emits a gamma-ray with energy 0.662 MeV. The AmBe source emits both gamma-rays and neutrons. The AmBe source runs were not done to determine the gain, but were done to check the PSD clarity and to identify problematic cells.

4.1.1 *Blowfish* Repairs and Updates

In September 2013 a new cell mounting technique was implemented; it consists of mounting the PMT's with aluminum collars, and using piano wire to hold the cell head and the PMT together.

During the mounting upgrade the cells were tested for light leaks and other possible issues. A few of the cells we found to contain large bubbles in the liquid scintillator containers; the bubbles in the cells decreases the efficiency, and alters the PSD properties of the cell. In addition, a few cells were found to have broken containers resulting in the leakage of the liquid BC-505. The corrupted cells were removed and sent for repair at the University of Virginia, where there are spare materials to construct additional cells. Additional problematic cells were identified with runs using the AmBe source during the July 2014 calibration runs.

These cells are not included in the analysis in this thesis, which is only concerned with cell gains. Most of these damaged cells have since been repaired or rebuilt.

4.1.2 Run List

We did a series of runs with a radioactive source placed, approximately, in the centre of the *Blowfish* detector. All of the runs, except a few, were done with standard settings of the high voltage. Some added runs were done to check the gain monitoring system under high voltage changes, see section 4.4. The optimal, or standard, high-voltage runs listed in table 4.1. Table 4.2 lists the runs when the high voltage was deliberately changed.

4.2 Stability of the Gain

The run data was processed as discussed in sections 2.3.4 and 3.1; we fitted the curves to determined the Compton edge and used this to determine the gain for each functioning cell, for all the July 2014 runs. The gains were plotted with respect to time, in hours during a particular day, see figures 4.1 to 4.12. The time shown on the plots are the start times for each run. The runs were generally about 20 minutes in length. All of the functioning cells were looked at, and a random selection of cells was chosen to display in this thesis. In the figures the solid horizontal line indicates the weighted mean of the gain values for that cell, during that day. Figures 4.1 to 4.12 show that the majority of the gains are stable within the uncertainty of the measured gain.

An exception might be noted for cell 9, see figures 4.1 and 4.5 where for some runs the gain is more than a few standard deviations away from the mean value. The Compton edge fitting for cell 9 during July 16, 2014 and July 17, 2014 was checked, and there was no evidence of a bad fit or a faulty cell. The measured gain values of cell 9 can be seen to be stable within uncertainty for July 19, 2014, see figure 4.9. Therefore the few data runs with with larger than normal deviations on July 16 and 17, can be attributed to statistical variations. In fact there is a lower count number for some cells on those days; this would lead to larger uncertainty in the gain determination.

We can conclude that there were no gain drift as a function of time during these calibration

45

Date	Run Number	Run Time (EST)
July 15, 2014	1546	17:22-17:30
	1547	19:19-19:32
July 16, 2014	1556	16:45-17:32
	1558	17:41-18:00
	1559	18:01-18:21
	1560	18:21-18:41
	1561	18:41-19:01
	1564	20:12-20:31
July 17, 2014	1566	10:47-11:07
	1567	11:07-11:27
	1568	11:30-11:51
	1570	12:17-12:37
	1571	13:11-13:30
	1572	13:34-13:53
	1573	13:55-14:15
	1574	14:16-14:36
	1575	14:46-15:06
	1576	15:08-15:27
July 19, 2014	1609	16:18-16:39
	1610	16:39-16:59
	1611	17:00-17:20
	1612	17:20-17:40
	1613	17:40-18:00

Table 4.1: Run list of Cesium-137 calibration runs done under standard detector settings.

Run Number	Run Time	High Voltage Alterations: *With Respect to the Standard Voltage Setting*
1615	18:09-18:30	+20 V
1616	18:30-18:50	+20 V
1617	18:56-19:15	-10 V
1618	19:15-19:33	-10 V
1619	19:36-20:16	-10 V
1620	20:17-20:37	-10 V

Table 4.2: Run list of Cesium-137 calibration runs, obtained July 19, 2014, with alterations to the standard high voltage settings

runs. This would be expected because there were no mechanical changes to *Blowfish*; no changes in the cell's high voltage setting; and there were no major changes in the count rates experienced for each cell. Recall from section 2.1.2, that large changes in count rate is known to possibly cause gain changes due to PMT fatigue. However, we know that in a normal experimental situation there is a possibility of a gain drifts. Therefore we look to the gain tracking system to make sure we can catch and correct these gain drifts. Before checking the gain tracking system we must first check the assumption, $R'_i = R_i$, that was made in section 3.2.2.
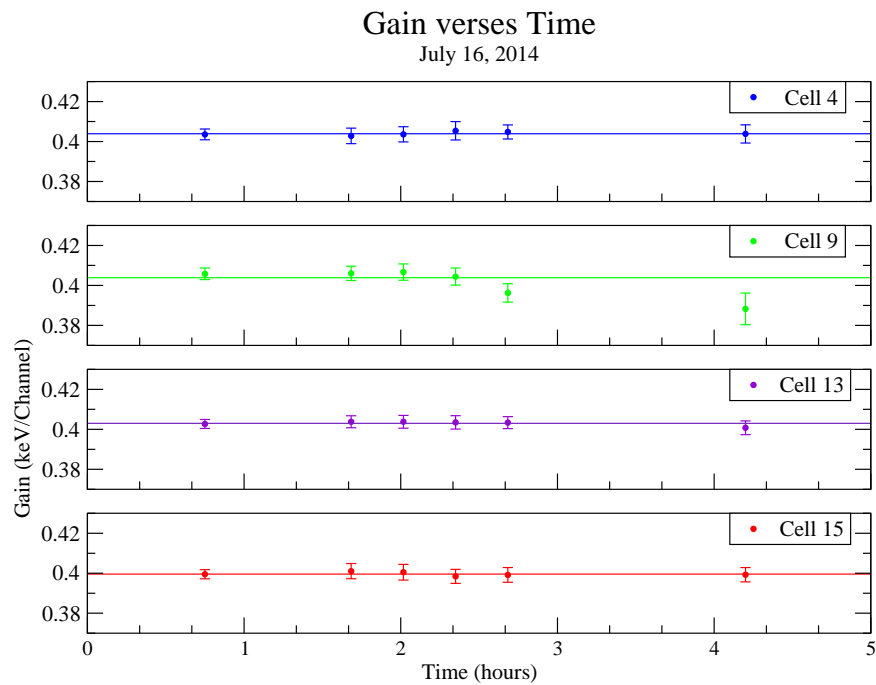
Figure 4.1: The measured gains and the weighted mean of the measured gain values as time progresses, on July 16, 2014, for cells 4, 9, 13, and 15.
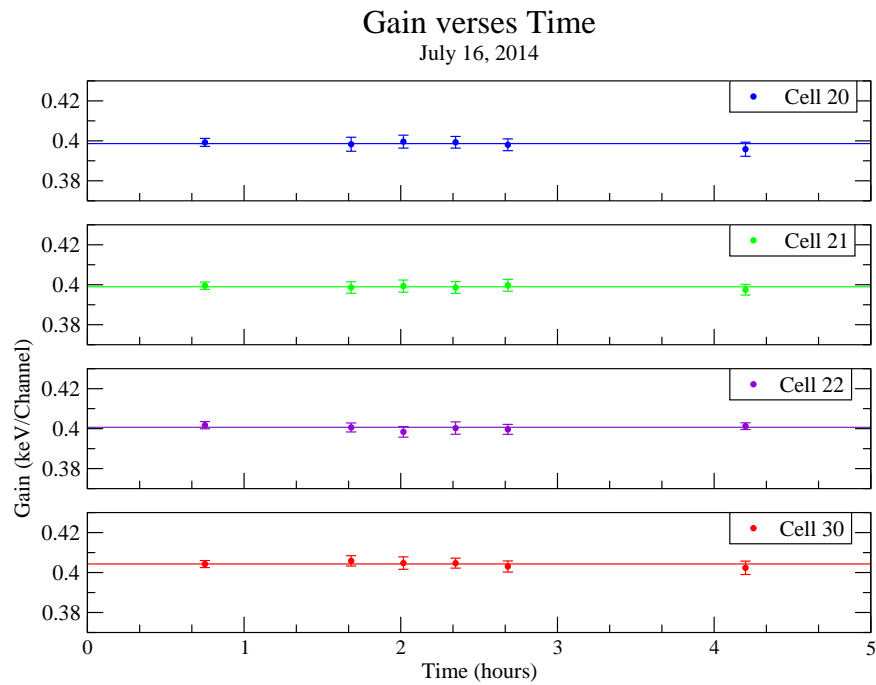

Figure 4.2: The measured gains and the weighted mean of the measured gain values as time progresses, on July 16, 2014, for cells 20, 21, 22, and 30.
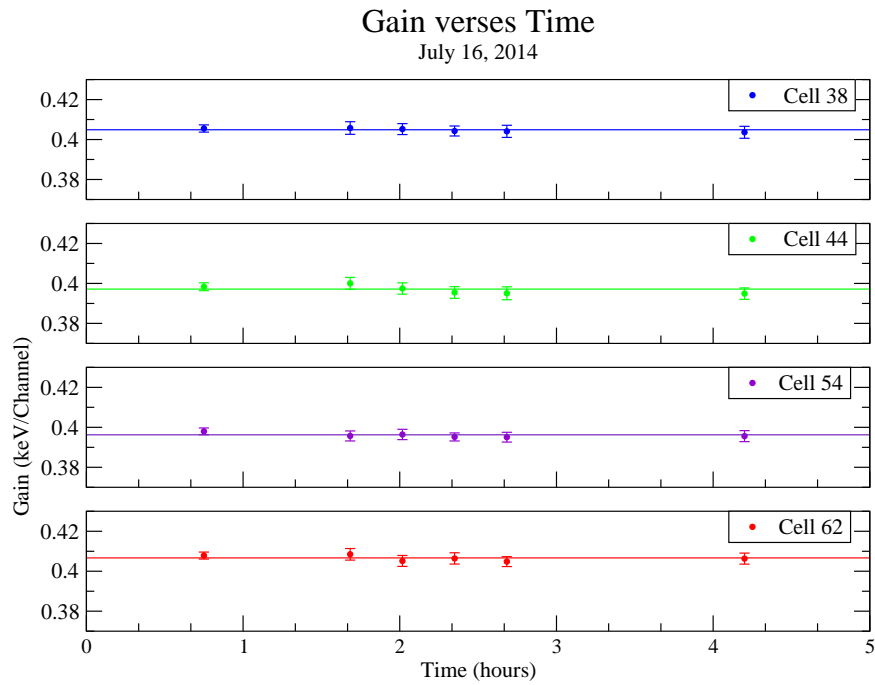
Figure 4.3: The measured gains and the weighted mean of the measured gain values as time progresses, on July 16, 2014, for cells 38, 44, 54, and 62.
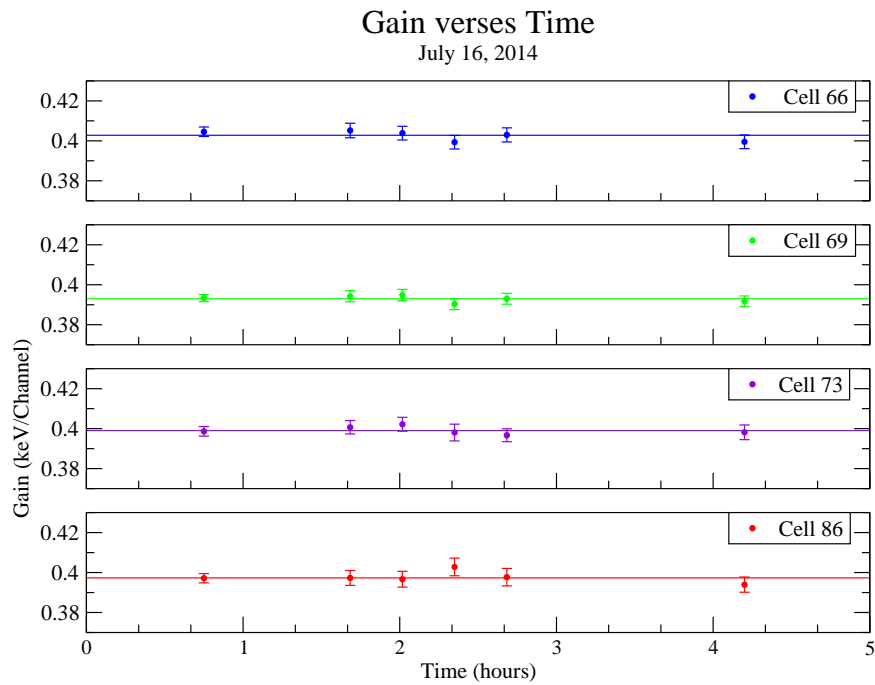

Figure 4.4: The measured gains and the weighted mean of the measured gain values as time progresses, on July 16, 2014, for cells 66, 69, 73, and 86.
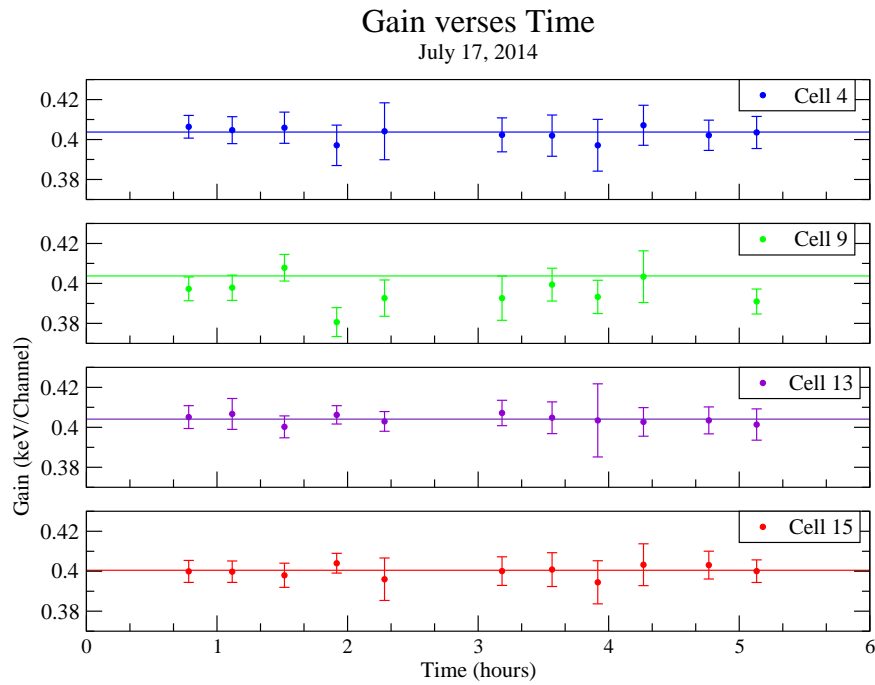
Figure 4.5: The measured gains and the weighted mean of the measured gain values as time progresses, on July 17, 2014, for cells 4, 9, 13, and 15.
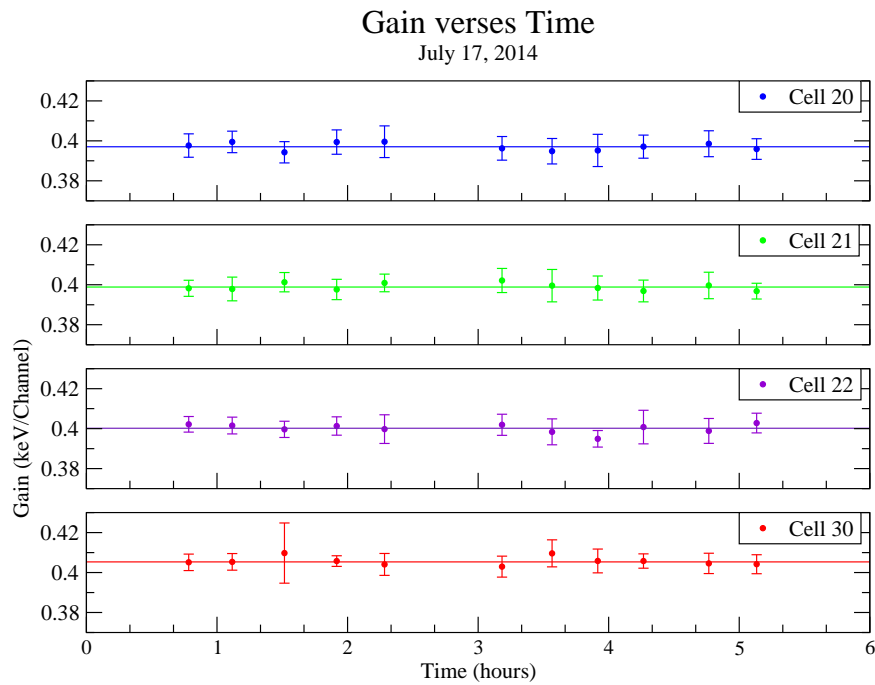

Figure 4.6: The measured gains and the weighted mean of the measured gain values as time progresses, on July 17, 2014, for cells 20, 21, 22, and 30.
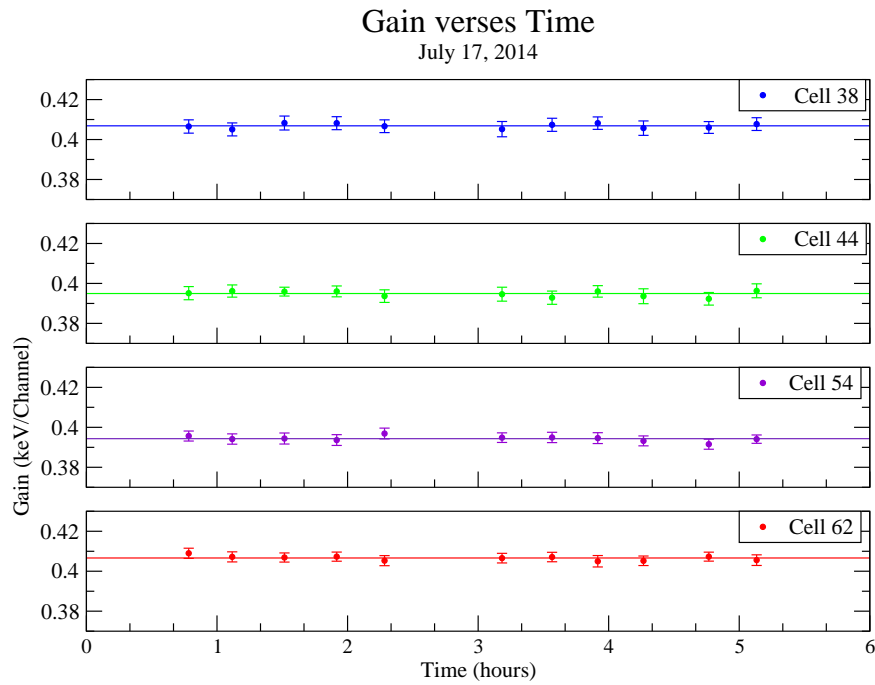
Figure 4.7: The measured gains and the weighted mean of the measured gain values as time progresses, on July 17, 2014, for cells 38, 44, 54, and 62.
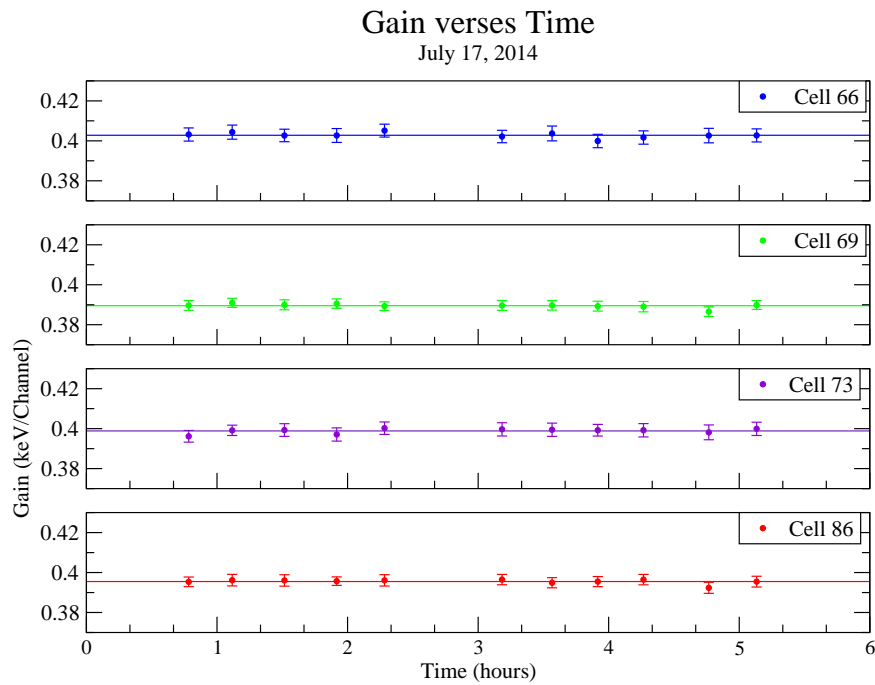

Figure 4.8: The measured gains and the weighted mean of the measured gain values as time progresses, on July 17, 2014, for cells 66, 69, 73, and 86.
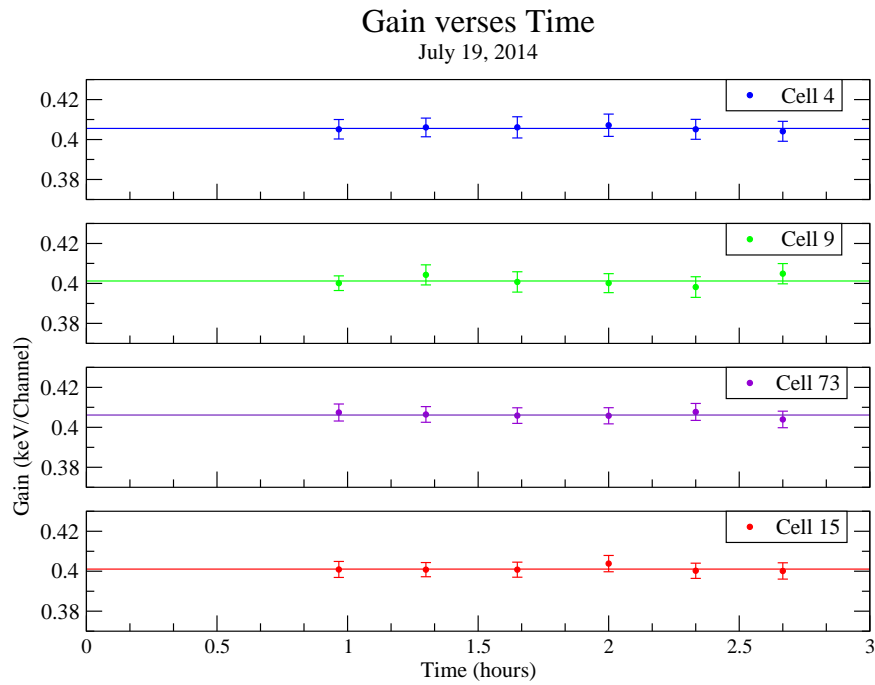
Figure 4.9: The measured gains and the weighted mean of the measured gain values as time progresses, on July 19, 2014, for cells 4, 9, 13, and 15.
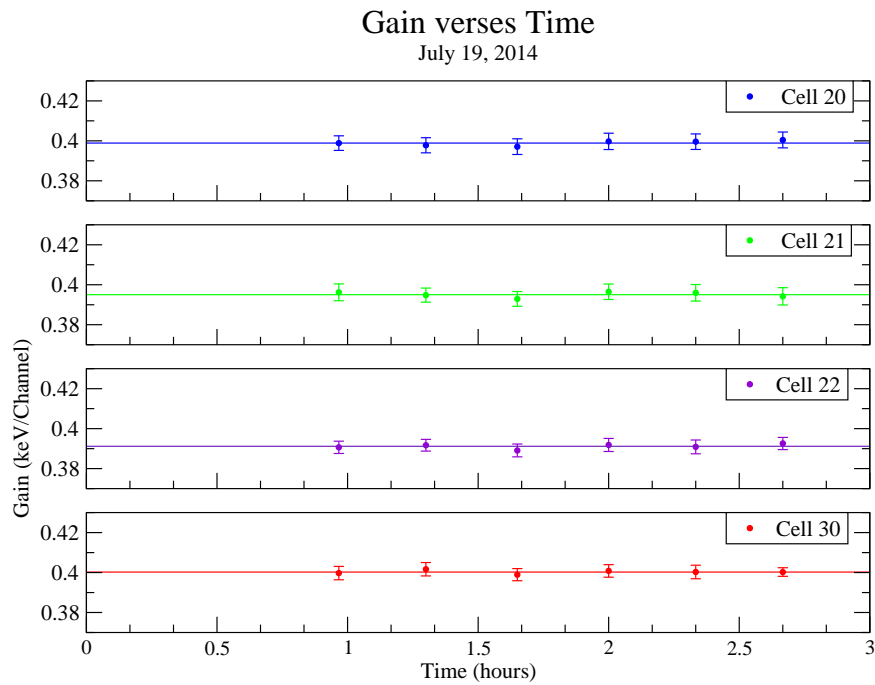

Figure 4.10: The measured gains and the weighted mean of the measured gain values as time progresses, on July 19, 2014, for cells 20, 21, 22, and 30.
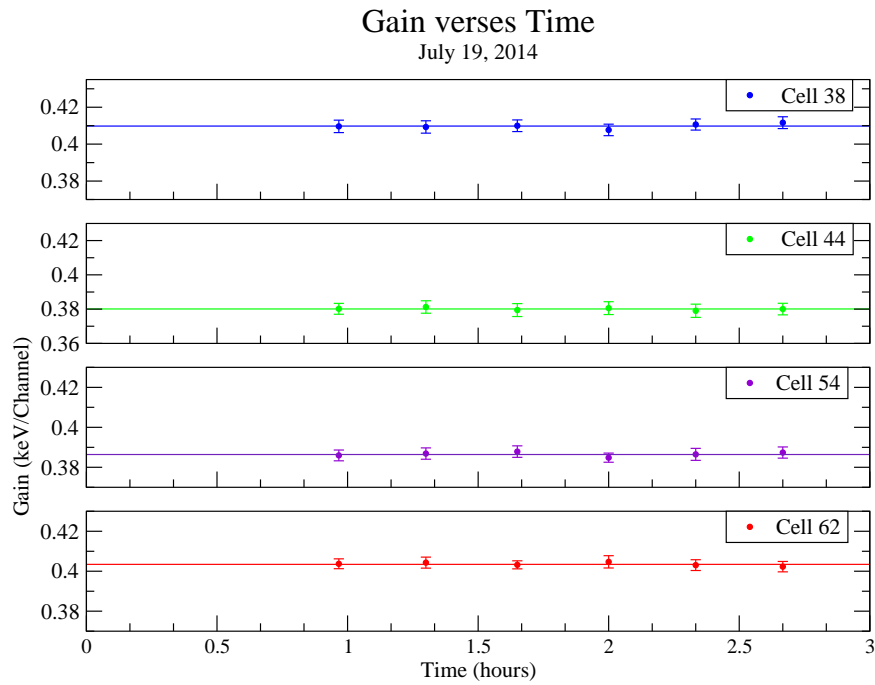
Figure 4.11: The measured gains and the weighted mean of the measured gain values as time progresses, on July 19, 2014, for cells 38, 44, 54, and 62.
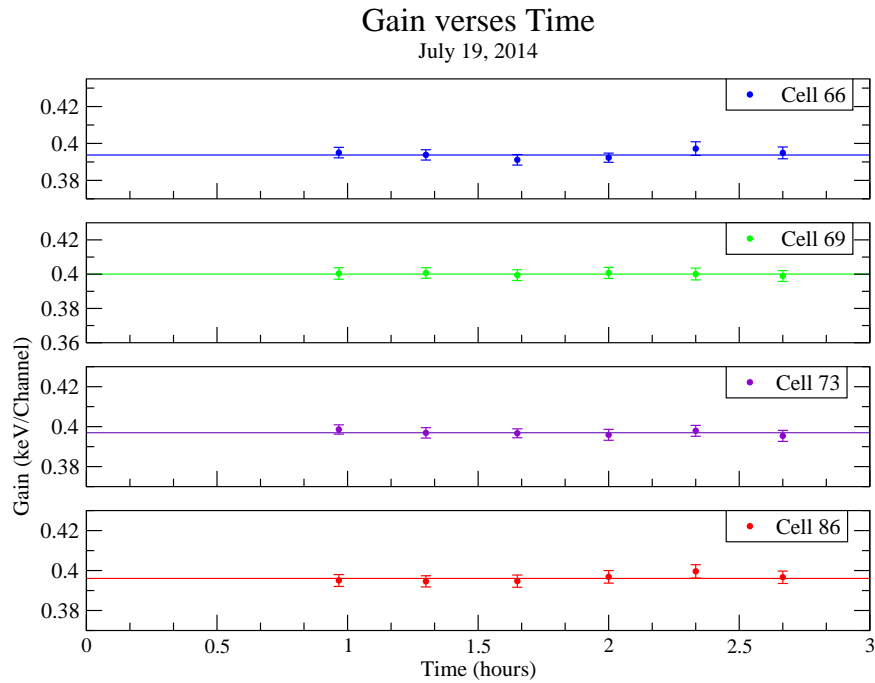

Figure 4.12: The measured gains and the weighted mean of the measured gain values as time progresses, on July 19, 2014, for cells 66, 69, 73, and 86.

4.3 Validity of the $R_i' = R_i$ Assumption

Recall the R-values are a ratio of the light transportation efficiency going to the cells and to the monitor detector. The R-values, R_i, were found using equation (3.11), for each cell in all of the runs for which flasher data was present. R_i is determined from a particular calibration run and is compared to the value calculated from an earlier calibration run [BPIW09]. Since the gain was calculated for all of the runs we can check to see how the R-values respond throughout the day. If there are no mechanical changes to the detector the assumption, $R_i' = R_i$, should be safe to make. Recall that this is the assumption that the gain prediction is based on, see section 3.2.2. Mechanical changes to the detector, e.g. by rotating the *Blowfish* array, could lead in a changes to the fibre optic cables. The four LED flashers are attached to 4 different *Blowfish* arms; a part of the light signal coming from the flasher LED is transported to each cell, and to the monitor detector. Any change in the light path, by either moving or twisting of the fibre optic cable, will lead to a difference in the later R-value, R_i'. So, $R_i' \neq R_i$, which means the gain cannot be predicted or tracked using the gain monitoring system. During the July 2014 calibration runs, we deliberately did not make any positional changes to the detector through the course of these days. Therefore we expect that the $R_i' = R_i$ assumption should be valid for these runs.

R-values vary from cell to cell, however, the R-values of each individual cell should remain constant as time progresses. Figure 4.13 is a demonstration of what the R-values look like for runs 1558, 1560, and 1564; these runs took place on July 16, 2014. The R-values for an individual cell plotted as a function of time help see how stable the $R_i' = R_i$ relationship is. Figures 4.14 to 4.17 contain the plots for the R-values as a function of run number and the R-average for that cell. The R-average is the weighted mean of the all of the R-values for a given cell, taken over all of the run numbers; tables 4.1 and 4.2 list all of the run numbers. Since the R-values vary from cell to cell, it is easier to look at the ratio of the R-value over R-average, $\frac{R-value}{R-average}$, (calculated over all of the present run numbers) for that particular cell, see figures 4.18 to 4.21.

We see that the R_i values are consistent over the span of the three days of our calibration runs. Therefore the assumption $R_i' = R_i$ can be made. The percentage range of $\frac{R_i}{R_{ave}}$ is
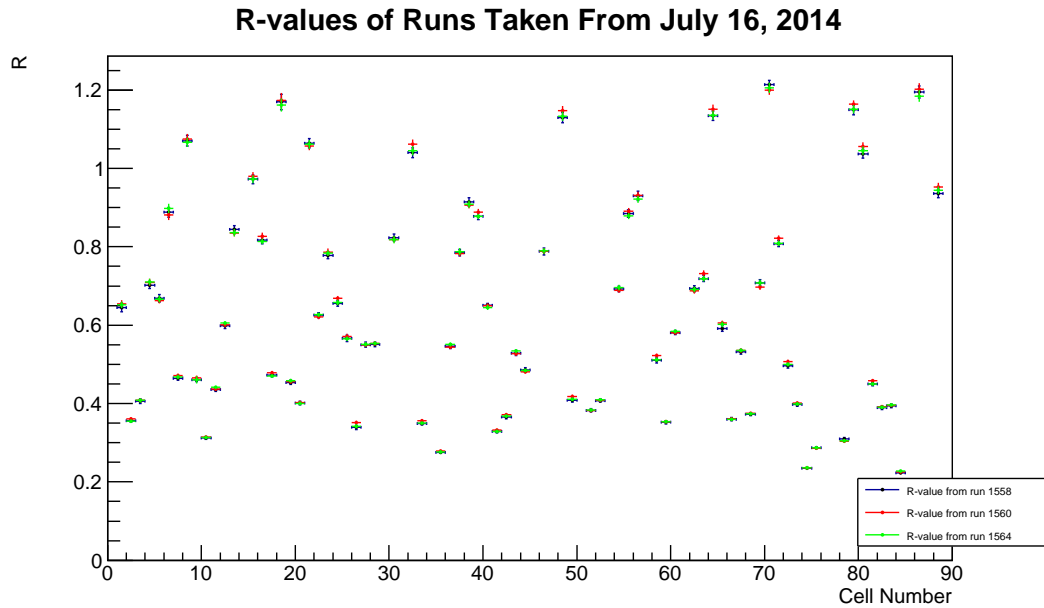
Figure 4.13: A plot of the R-values of all of the functioning cells, for runs 1558, 1560, and 1564; these runs took place on July 16, 2014.
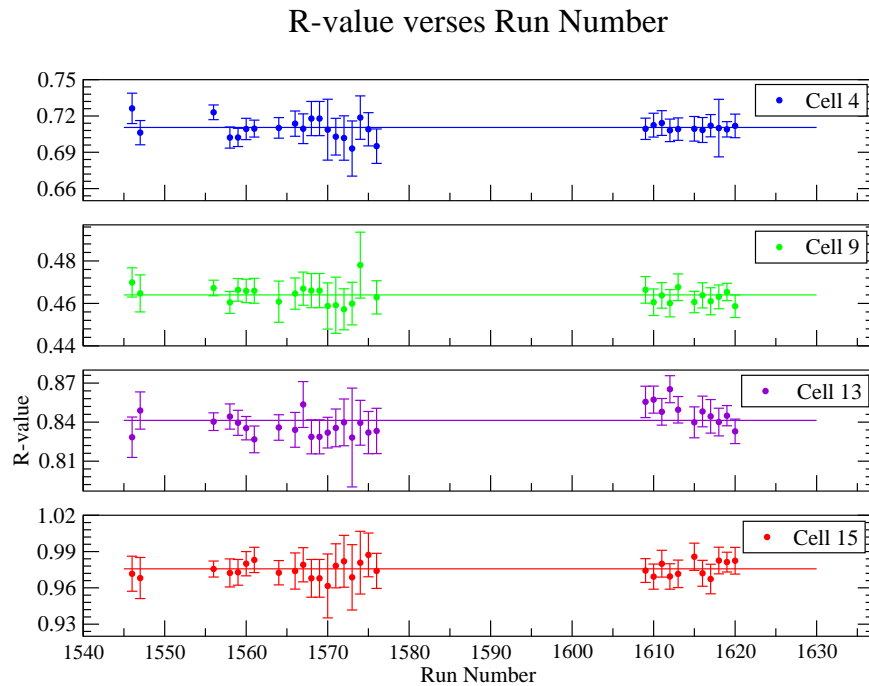

Figure 4.14: The R-values as a function of run number, plotted against the weighted mean of R for cells 4, 9, 13, and 15. The run numbers are as detailed in tables 4.1 and 4.2.
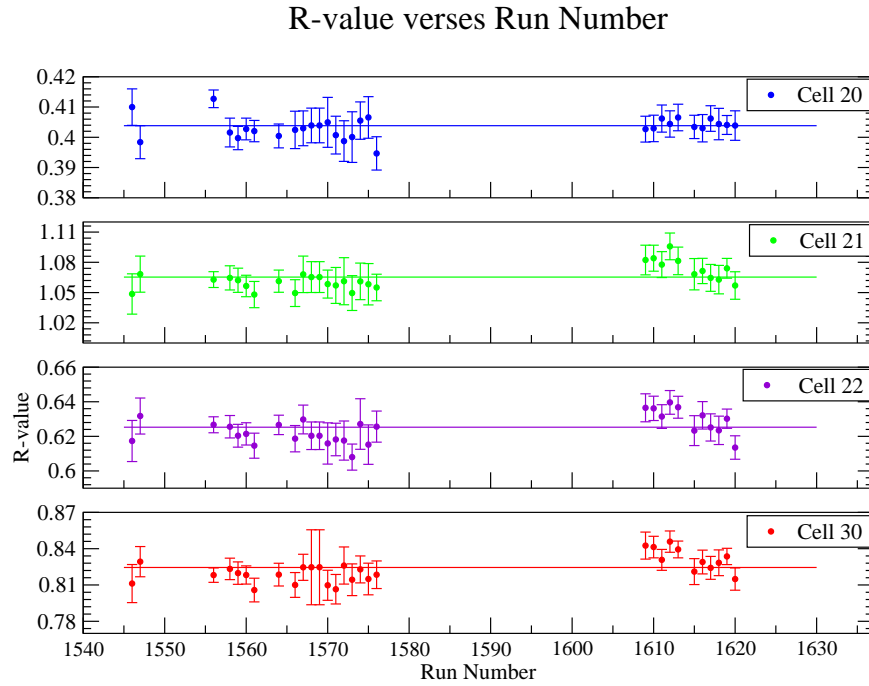
Figure 4.15: The R-values as a function of run number, plotted against the weighted mean of R for cells 20, 21, 22, and 30. The run numbers are as detailed in tables 4.1 and 4.2.
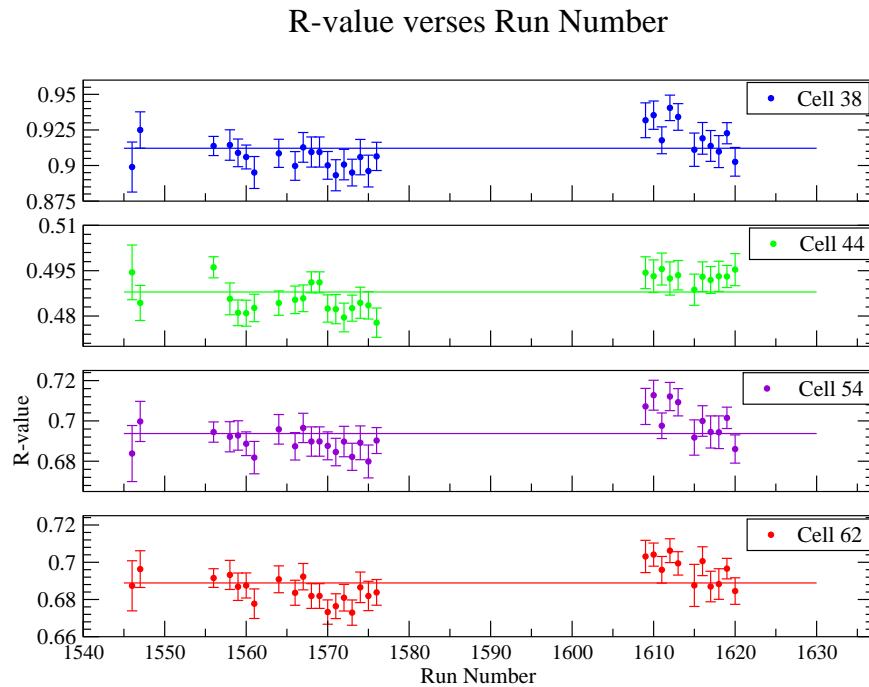

Figure 4.16: The R-values as a function of run number, plotted against the weighted mean of R for cells 38, 44, 54, and 62. The run numbers are as detailed in tables 4.1 and 4.2.
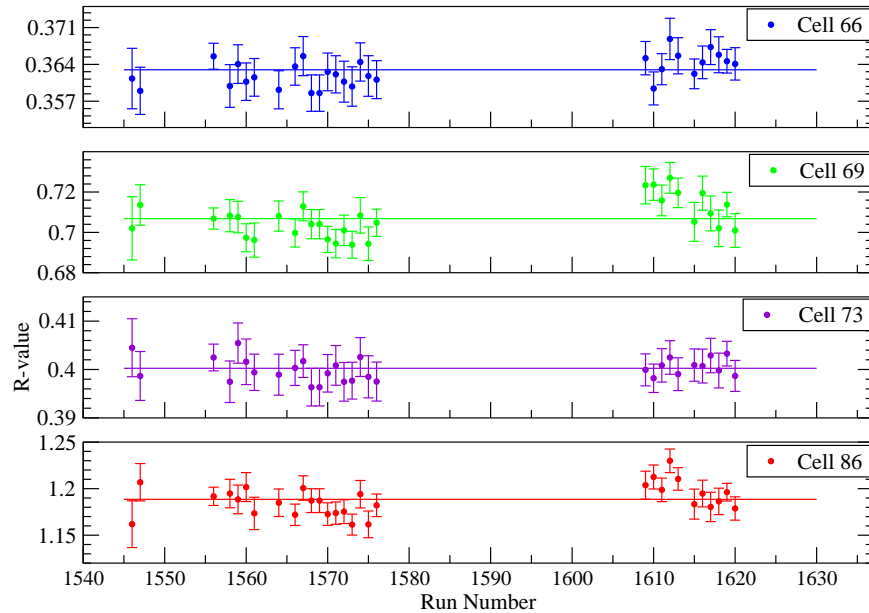
Figure 4.17: The R-values as a function of run number, plotted against the weighted mean of R for cells 66, 69, 73, and 86. The run numbers are as detailed in tables 4.1 and 4.2.

the percentage range in which the gain will be tracked. It is important to look at the run numbers associated with the, deliberate, alteration of the high voltage (these are runs 1615 to 1620, see section 4.4 and table 4.2). We see from figures 4.18 to 4.21 that the R-value are stable, within uncertainty, even for runs where a high voltage change was made.

Our conclusion that $R_i' = R_i$ is only valid when there are no position changes of the *Blowfish* detector. If, in future experiments, the detector's position is changed, the movement should be noted, and a new calibration run should be done.

Since, for our calibration runs, the assumption of $R_i' = R_i$ is valid, the gain prediction and gain tracking system can be used and tested.

4.4   Altering the High Voltage

The high voltage setting was intentionally changed to examine how well the gain monitoring system can track the changes to the gain that results.

We know that we can change the gain by altering the high voltage. Figures 4.22, 4.23,

Figure 4.18: Ratio of R-value to the weighted mean of R plotted against the run number for cells 4, 9, 13, and 15. The run numbers is as detailed in tables 4.1 and 4.2.

Figure 4.19: Ratio of R-value to the weighted mean of R plotted against the run number for cells 20, 21, 22, and 30. The run numbers is as detailed in tables 4.1 and 4.2.

Figure 4.20: Ratio of R-value to the weighted mean of R plotted against the run number for cells 38, 44, 54, and 62. The run numbers is as detailed in tables 4.1 and 4.2.
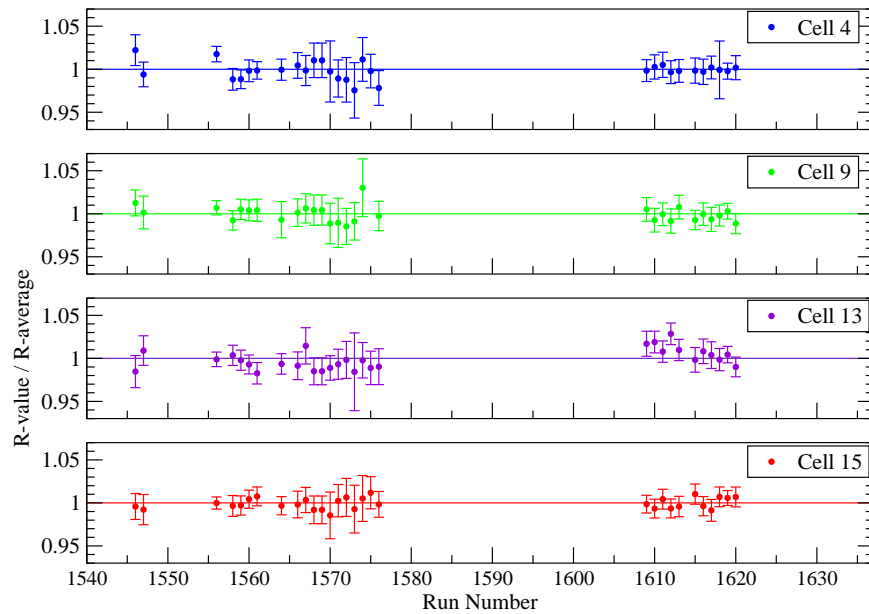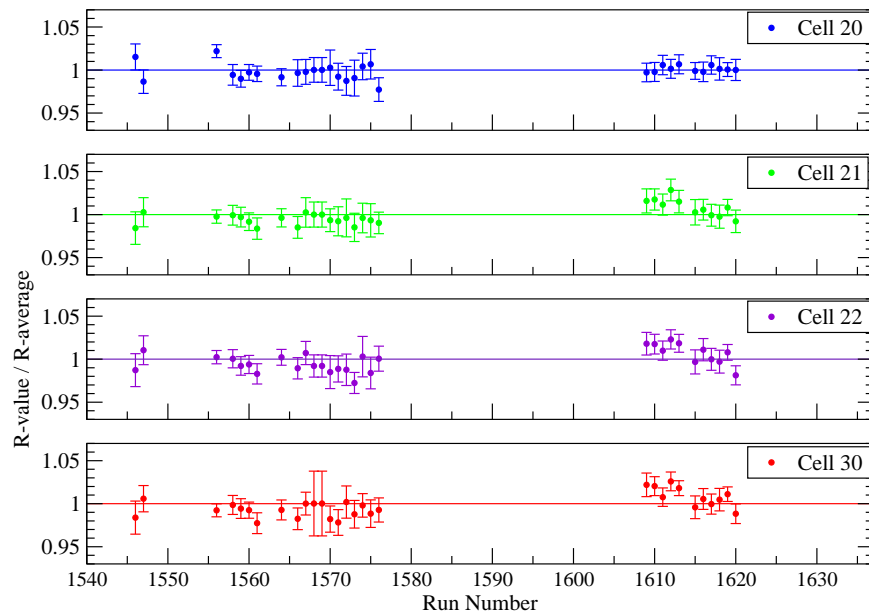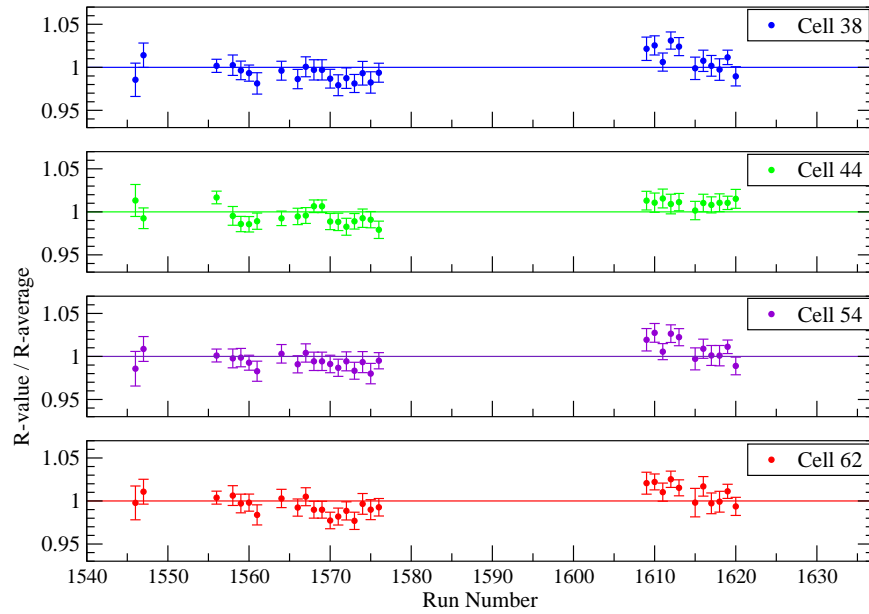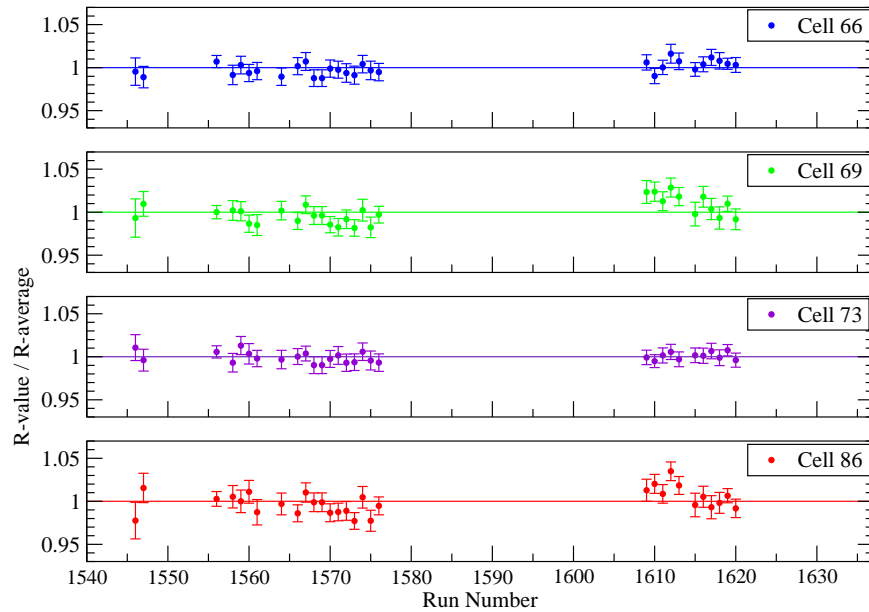

Figure 4.21: Ratio of R-value to the weighted mean of R plotted against the run number for cells 66, 69, 73, and 83. The run numbers is as detailed in tables 4.1 and 4.2.

Figure 4.22: Gain plot as a function of run number, for cells 4, 9, 13, and 15 for July 19, 2014, high voltage alteration runs(see table 4.2).

4.24, and 4.25, show how the gain responded to the high voltage change. As the voltage increased the gain also increased; and as the voltage was decreased the gain also decreased. The 2 earlier run numbers, 1613 and 1612, are with the standard high voltage settings have gains that are between the decreased and increased high voltage settings. Recall, section 2.1.2, the high voltage setting has an affect on the PMT and the output current pulse. The output current pulse is what the ADC converts into a number read by the DAQ. A change in the high voltage, changes the PMT's dynode potentials resulting in a gain change. It is also known that the PMT takes time to warm up when the applied high voltage is initially turned on. These alterations to the gain are what the gain monitoring system is designed for.

Figure 4.23: Gain plot as a function of run number, for cells 20, 21, 22, and 30 for July 19, 2014, high voltage alteration runs(see table 4.2).

Figure 4.24: Gain plot as a function of run number, for cells 38, 44, 53, and 62 for July 19, 2014, high voltage alteration runs(see table 4.2).
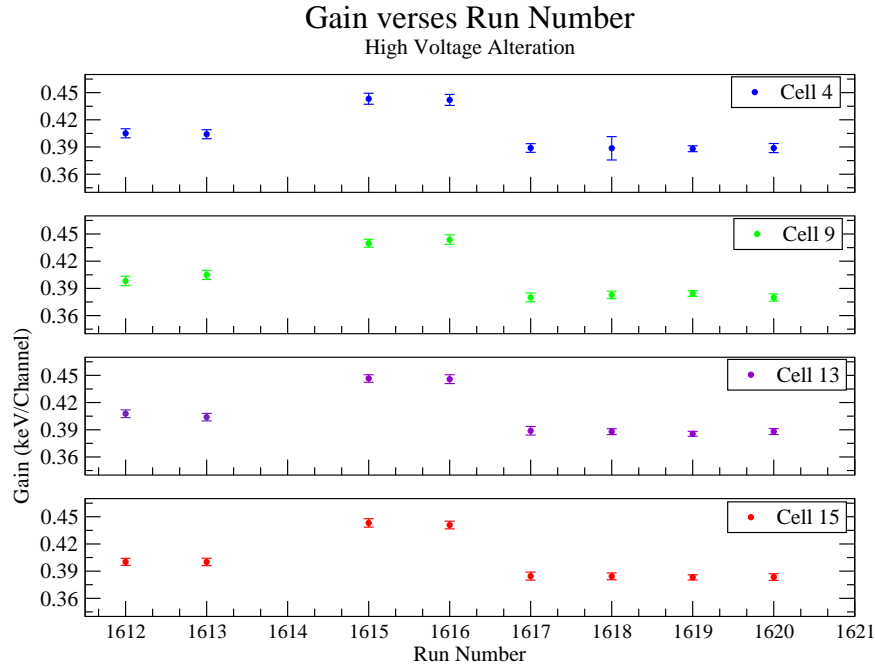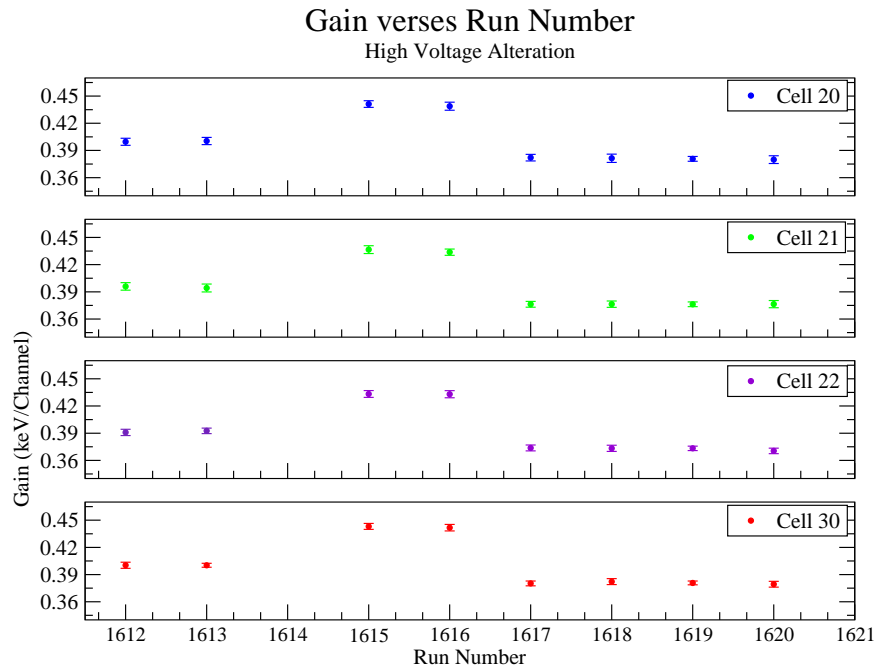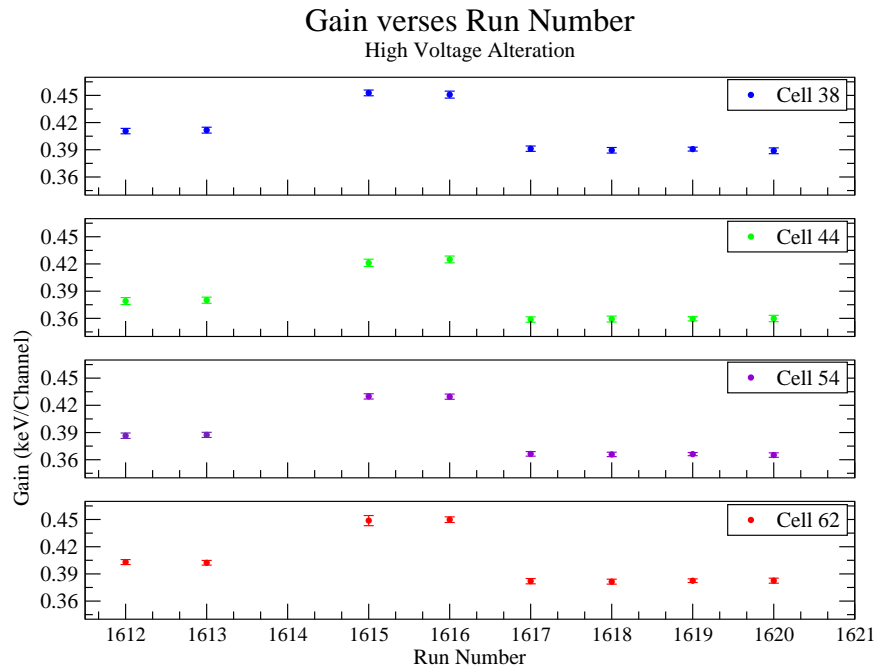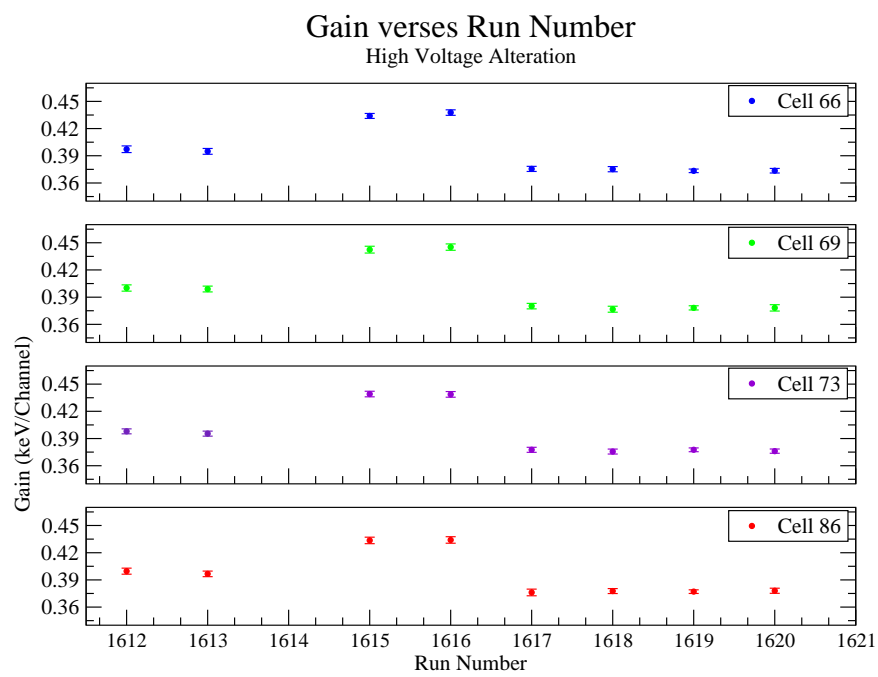
Figure 4.25: Gain plot as a function of run number, for cells 66, 69, 73, and 86 for July 19, 2014, high voltage alteration runs(see table 4.2).

4.5 Gain Tracking

Since we've seen that the R-value assumption is a valid assumption, we can use equation (3.16) to predict the gain. Gain prediction uses a measured, gain calibration run, and the R-value, R_i, derived from it, to determine what the the gain will be in a later run, g_i'. The purpose of this section is to make sure the predicted gain is valid during our calibration runs. If the gain monitoring system is able to track slight fluctuations and can track the gain under stress, e.g. by high voltage changes, then the system can be trusted to track the gain values in further experiments.

The gains were predicted using the measured gain values obtained from an early calibration run; this is referred to as a base run. This base run provides the R-values that are used in equation (3.16), giving us the predicted gain, also referred to as the calculated gain. The statistical uncertainty in the measured R_i, g_m', A_{Fm}' and A_{Fi}' are included in the calculation of the uncertainty in the predicted gain, g_i' [BPIW09].

In order to determine how the gain can be predicted and tracked, the measured and calculated gains are compared to one another; the ratio of the calculated and measured gain is plotted for each run number. Ideally the ratio of the calculated gains to the measured gains should be 1.

Figures 4.30 and 4.31 show that the ratio of the calculated gains to the measured gains are all stable, within the uncertainties. Even when the system was intentionally put under stress, by making deliberate changes in high voltage, the ratio does remain equal to 1 within uncertainties. This means the the gain monitoring system was able to predict the gain even when the high voltage was changed.

The results of this section show that the calculate gain is always within a few percent of the true gain.

Figure 4.26: Ratio of the calculated gains with respect to the measured gains. Run 1556 was used as the base run to find the calculated gains for runs 1558, 1559, 1560, and 1561.

Figure 4.27: Ratio of the calculated gains with respect to the measured gains. Run 1556 was used as the base run to find the calculated gains for run 1564, and run 1566 was used as the base run to find the calculated gains for runs 1567, 1568, and 1570.

Figure 4.28: Ratio of the calculated gains with respect to the measured gains. Run 1566 was used as the base run to find the calculated gains for runs 1571, 1572, 1573, and 1574.

Figure 4.29: Ratio of the calculated gains with respect to the measured gains. Run 1566 was used as the base run to find the calculated gains for runs 1575 and 1576, and run 1609 was used as the base run to find the calculated gains for runs 1610 and 1611.
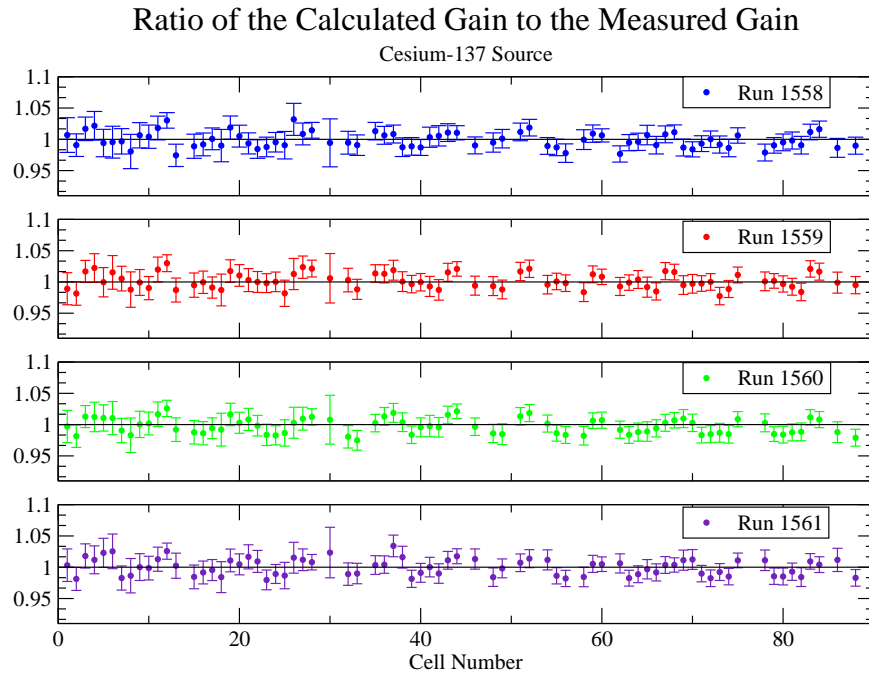
Figure 4.30: Ratio of the calculated gains with respect to the measured gains. Run 1609 was used as the base run to find the calculated gains for runs 1612 and 1613, and run 1613 was used as the base run to find the calculated gains for runs 1615 and 1616.
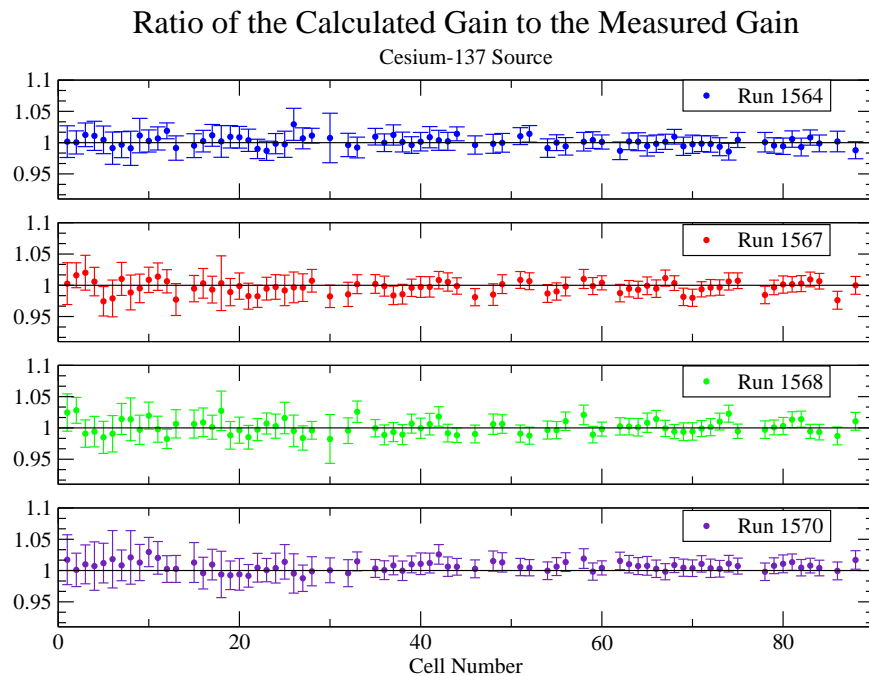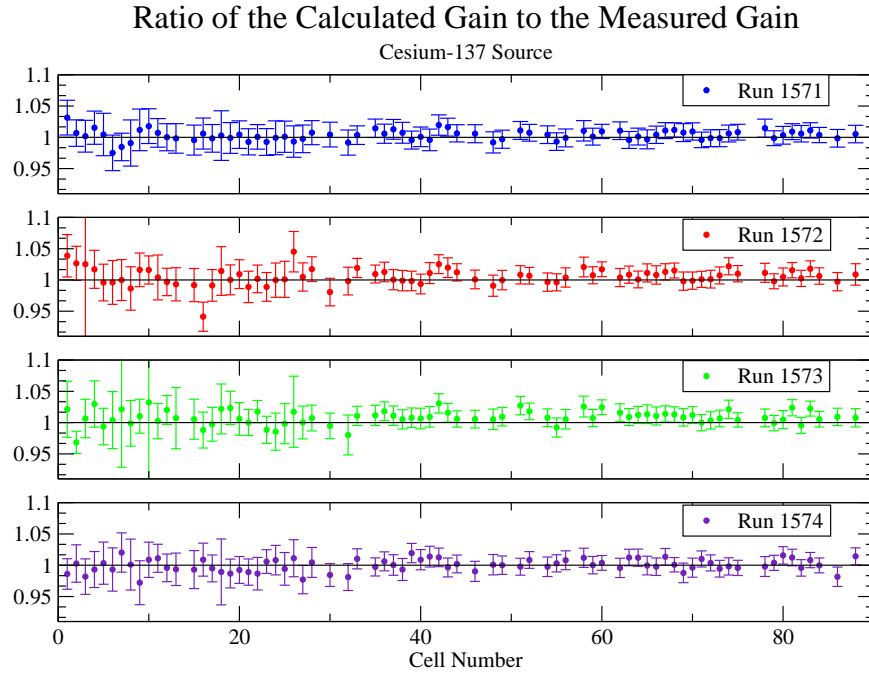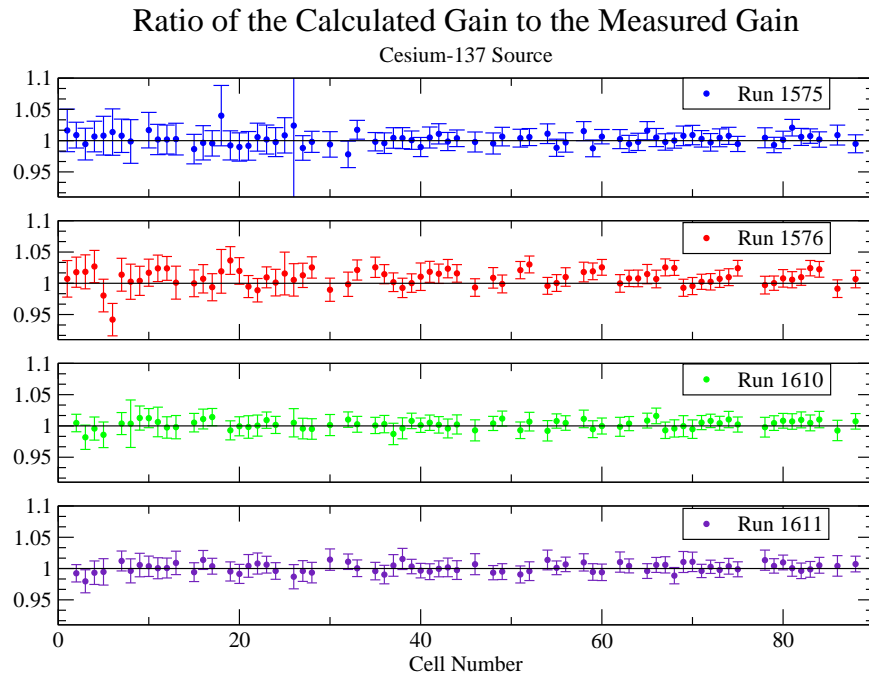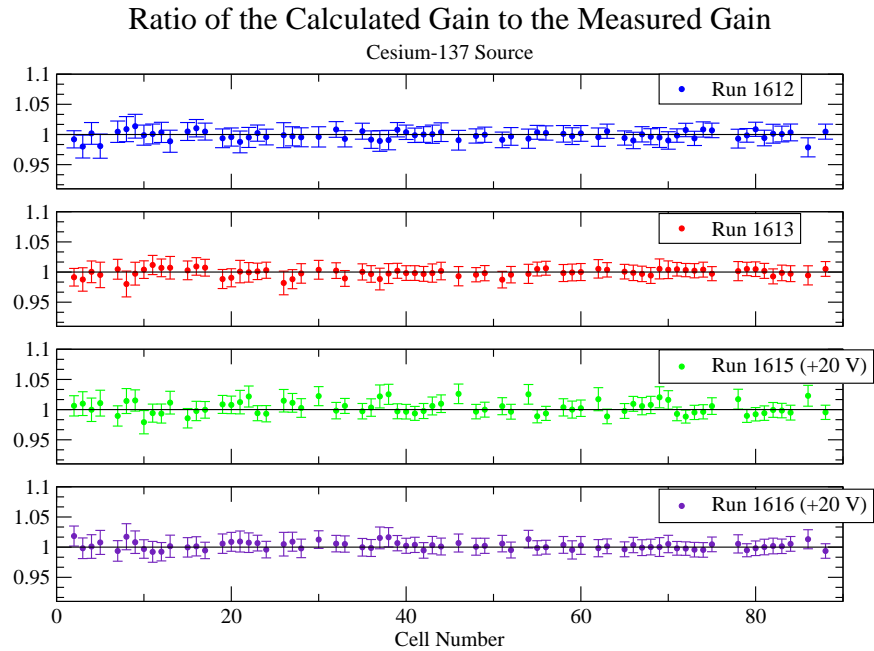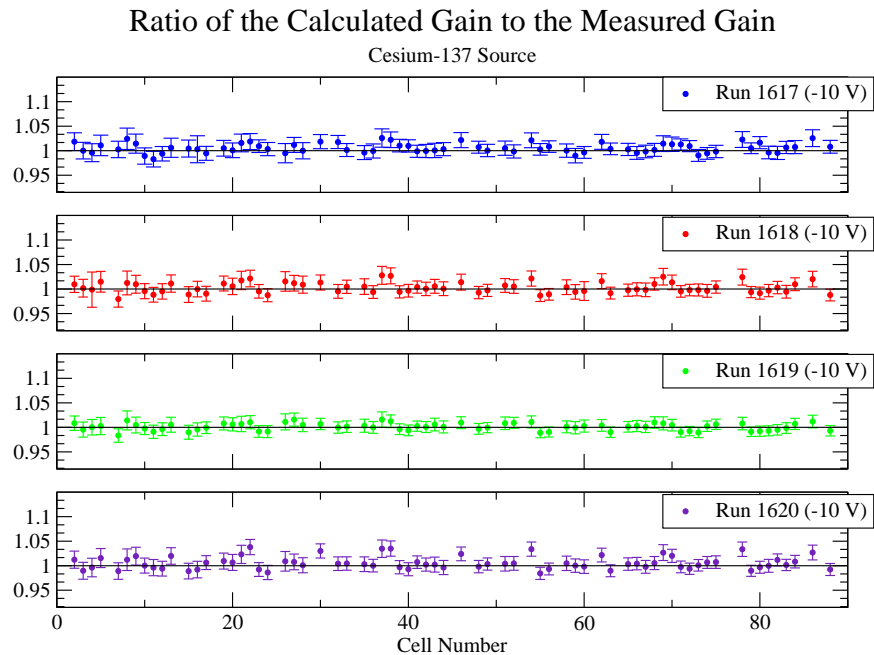

Figure 4.31: Ratio of the calculated gains with respect to the measured gains for run numbers. Run 1613 was used as the base run to find the calculated gains for runs 1617, 1618, 1619, 1620.

4.6 Neutron Yield

Recall, the neutron yield is dependent on the efficiency of the detector, ϵ. As discussed in section 1.2 the placement of the minimum light output cut is an important factor in determining the efficiency of the detector. Smaller incident gamma-ray energies, result in smaller kinetic energies of emitted neutrons from a photoneutron reaction, and therefore smaller light output from the detectors. Therefore, for the lower the gamma-ray energy, the placement of the minimum light output cut becomes that much more important in determining the efficiency of the detector.

An uncertainty in the gain is equivalent to an uncertainty in the placement of the light output threshold. We wish to determine how big an effect an uncertainty in the gain has on the efficiency for detecting neutrons. To determine this relation we use the GEANT4 simulation of the *Blowfish* detector. The simulation was run for photodisintegration of the deuteron with gamma-ray energies of 6 MeV, 10 MeV and 20 MeV. This covers the range of energies that will be used in the GDH experiment. In the simulation *Blowfish* was in the GDH orientation and the target was HIFROST. The angular distribution used in the simulation were the theoretical prediction of Schwamb and Arenhövel [SA01].

In the analysis of the simulation output data, the minimum light output cut was set, and the yield of neutrons from each *Blowfish* cell was determined by integrating the light output spectrum above that minimum light output cut. Then, the same simulation data was analyzed using a minimum light output cut that was decreased by 1%. The yields determined from this procedure are plotted in figures 4.32, 4.33 and 4.34. The minimum light output cuts used in this analysis (shown in the figures) are typical values that might be used in the analysis of real data in the GDH experiment. The values are those expected to provide a good compromise between a value low enough to produce sufficient counts, and high enough to maintain good pulse shape discrimination (PSD) between neutron and gamma-rays.

4.6.1 Percent Uncertainty in Yield

The percent uncertainty in the yield is the percent change in yield resulting in a 1% change in the minimum light output cut (threshold). These are plotted per cell in Figure 4.35.

Figure 4.32: The neutron yield for deuteron photodisintegration at a gamma-ray energy of 6 MeV, at two different minimum light output cuts.
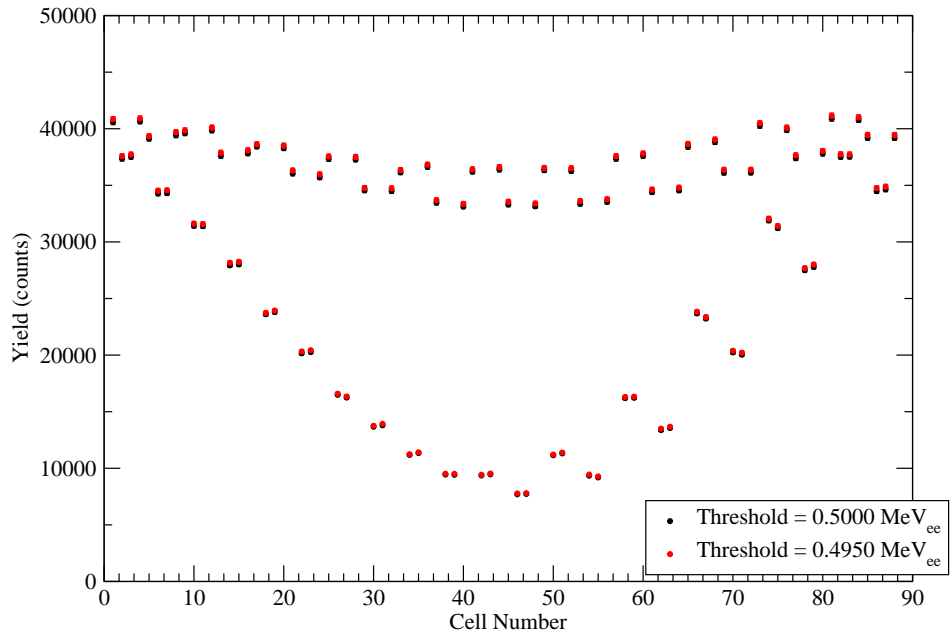
Figure 4.33: The neutron yield for deuteron photodisintegration at a gamma-ray energy of 10 MeV, at two different minimum light output cuts.
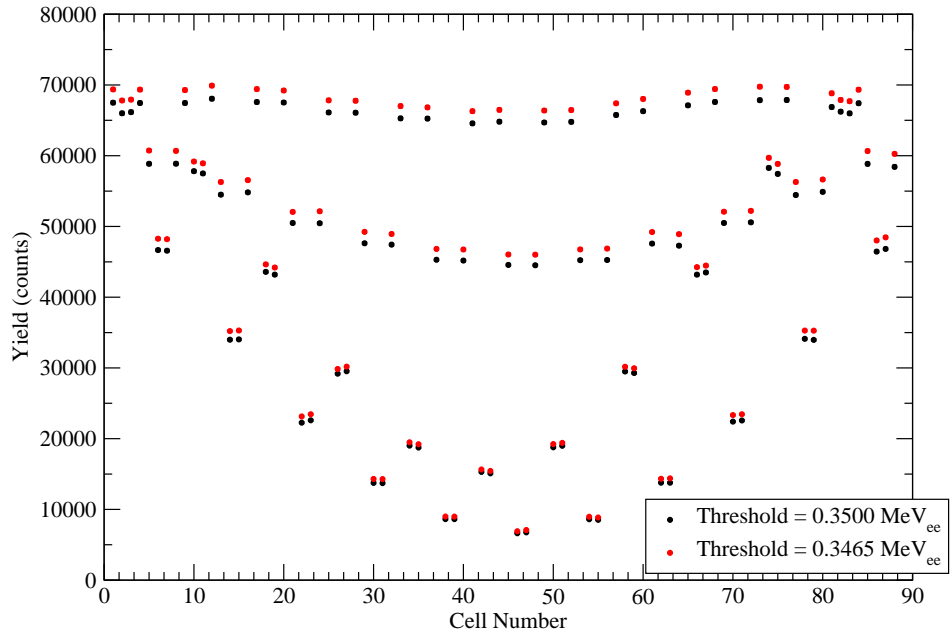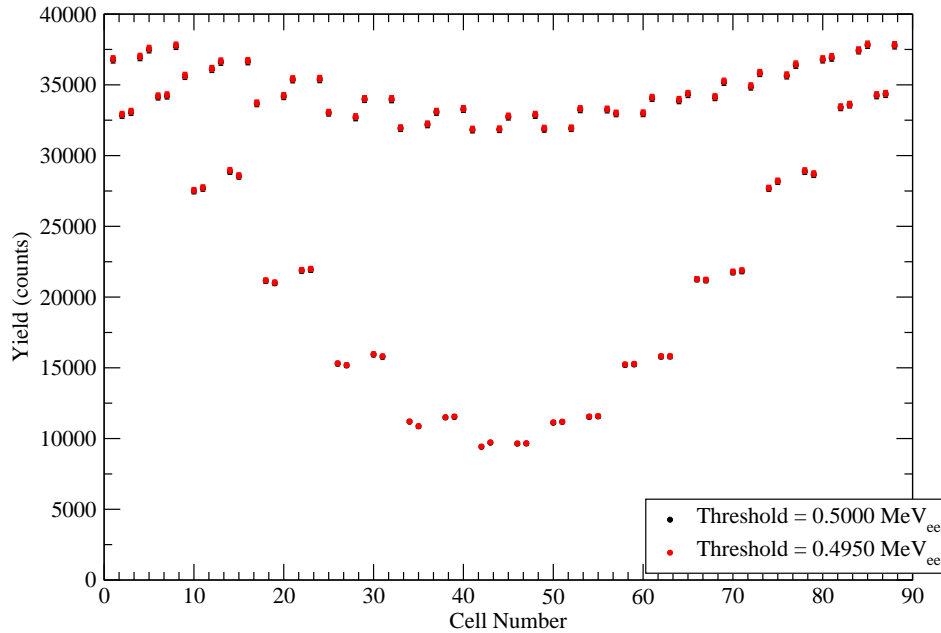
Figure 4.34: The neutron yield for deuteron photodisintegration at a gamma-ray energy of 20 MeV, at two different minimum light output cuts.

We see that an uncertainty in the gain has the largest effect on the uncertainty in the yield when the neutron energies are lowest, which is when the gamma-ray energy is lowest (6 MeV). This is when a smaller fraction of the neutrons produce light outputs that are above the minimum light output threshold.

From the previous section, we have established that we can determine the gain of a particular cell to within a few percent of the true gain. For the lowest gamma-ray energy of 6 MeV the uncertainty in the yield for a 1% uncertainty in gain is between 2% and 4.5%. Therefore, since the uncertainty in the gain may up to about 3%, the uncertainty in the yield of a cell could be as much as about 12%. For the gamma-ray energies of 10 MeV and 20 MeV the percent uncertainty in the yield, for a 1% uncertainty in the gain are less than 1%, so the effect on cell yield would be correspondingly less for these energies.

For the gamma-ray energy of 6 MeV, the above numbers would suggest that we would only be able only be able to determine a cross section to about 12% accuracy, which would be unacceptably large.

However, the situation is not as bad as that. In the analysis of an experiment the cross
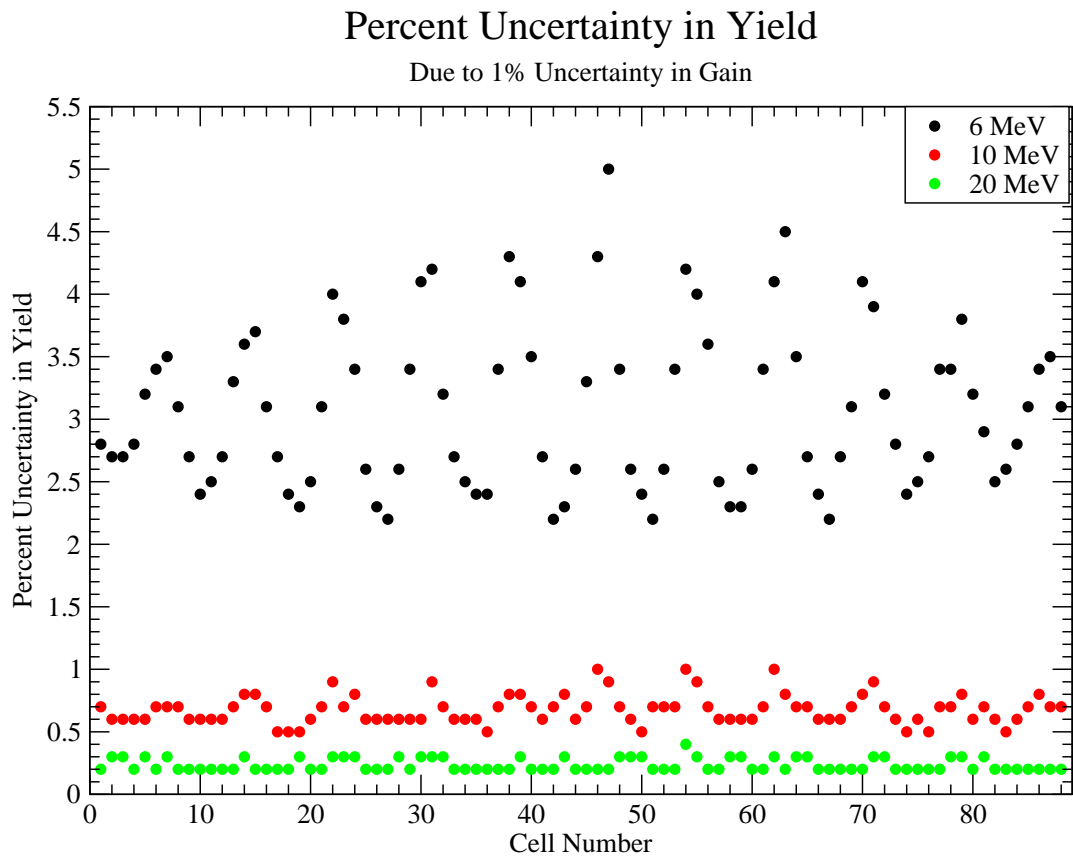
Figure 4.35: Percent Uncertainty in the Yield for 1% uncertainty in gain. For the photodisintegration of Deuterium where E_γ = 6 MeV, 10 MeV and 20 MeV; at light output thresholds of 0.350 MeV$_{ee}$, 0.500 MeV$_{ee}$ and 0.500 MeV$_{ee}$ respectively.

section is determined by a fit to the yields from all 88 cells in *Blowfish*. The fit function is the yields for each cell calculated using the simulation using a function for the angular distribution determined by the differential cross section

$$\frac{d\sigma}{d\Omega}(\theta) = A \left[1 + \sum_{k=1}^{4} a_k P_k^0(cos\theta) \right] \tag{4.1}$$

where P_k^0 are associated Legendre polynomials, a_k are parameters describing the angular distribution, and the parameter A can be related to the total cross section.

If our uncertainty in the gains were such that the our assumed gains were all shifted from the true gains in the same direction for all 88 cells, then our error in the cross section would be the same as our uncertainty in the yields. For example, at a gamma-ray energy of 6 MeV, our measured cross section could be up to 12% different from the true value. However, since the gains for each cell are determined independently, it is very unlikely that the gain error for each cell will be correlated with other cells.

To investigate the effect that independent gain shifts would have on a total cross section, the simulated yield for each cell was smeared with a Gaussian distribution. As a worst case, we chose a distribution with a standard deviation that was 15% of the yield in each cell. So, for a cell with simulated yield N, a random number was chose from a Gaussian distribution, centred on zero, with a standard deviation $0.15N$, and this was added to the cell's yield.

Figure 4.36 shows the simulated neutron yield for each cell, and for a neutron yield smeared with a 15% uncertainty. A fit to the smeared yield was made to determine the change, if any, on the fit parameter A. Even under this maximum duress of a 15% uncertainty in the yields for each cell, the fitted A parameter only changed by 1%. So even under the most extreme case, the total cross section measurement can be done so within a reasonable uncertainty.

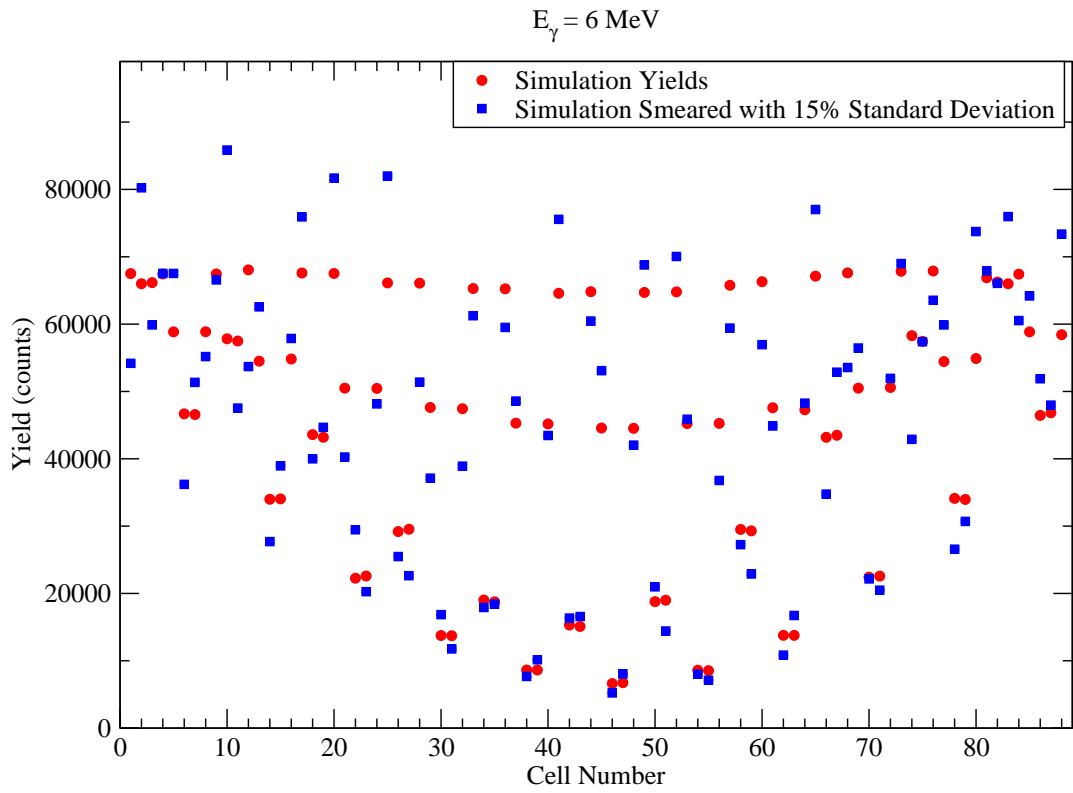**Figure 4.36:** The simulated neutron yield for deuteron photodisintegration at a gamma-ray energy of 6 MeV.

CHAPTER 5

CONCLUSION

The gains under our experimental conditions are more stable than we expected. This is extremely promising because there are some experimental settings where the gain monitoring system cannot be used. When the gain monitoring system cannot be used to track the gains, calibration runs need to be done more frequently. The gain monitoring system also performed excellently. The predicted gains were within 3% of the true gains; even when there were deliberate high voltage changes. The gain monitoring system helps maintain uncertainties at a normal level. We used the uncertainties found to see what affect they have on the total cross section. We found that even when the standard deviation was set at 15%, which was higher than we measured, the affect on the total cross section was a reasonable 1%.

The five-paddle flux monitor was repaired and tested during the September 2013 HIGS visit. Since then, the five-paddle flux monitor has successfully been used at the HIGS facility.

In the future, it is important to test the functionality of the repaired cells. The repaired cells will be tested for light leaks, clear PSDs, and consistent gain values. Calibration runs should also be done at the start and end of each day to ensure that the detector and the gain monitoring system is working for all of the cells. The tests performed for this thesis were completed while the accelerator was not running. Therefore, it would be beneficial to test the gain calibration while the accelerator is on to see if there are any discrepancies in the gains and the gain tracking system.

References

[AAA+03] S. Agostinelli, J. Allison, K. Amako, J. Apostolakis, H. Araujo, P. Arce, M. Asai, D. Axen, S. Banerjee, G. Barrand, F. Behner, L. Bellagamba, J. Boudreau, L. Broglia, A. Brunengo, H. Burkhardt, S. Chauvie, J. Chuma, R. Chytracek, G. Cooperman, G. Cosmo, P. Degtyarenko, A. Dell'Acqua, G. Depaola, D. Dietrich, R. Enami, A. Feliciello, C. Ferguson, H. Fesefeldt, G. Folger, F. Foppiano, A. Forti, S. Garelli, S. Giani, R. Giannitrapani, D. Gibin, J.J. Gmez Cadenas, I. Gonzlez, G. Gracia Abril, G. Greeniaus, W. Greiner, V. Grichine, A. Grossheim, S. Guatelli, P. Gumplinger, R. Hamatsu, K. Hashimoto, H. Hasui, A. Heikkinen, A. Howard, V. Ivanchenko, A. Johnson, F.W. Jones, J. Kallenbach, N. Kanaya, M. Kawabata, Y. Kawabata, M. Kawaguti, S. Kelner, P. Kent, A. Kimura, T. Kodama, R. Kokoulin, M. Kossov, H. Kurashige, E. Lamanna, T. Lampn, V. Lara, V. Lefebure, F. Lei, M. Liendl, W. Lockman, F. Longo, S. Magni, M. Maire, E. Medernach, K. Minamimoto, P. Mora de Freitas, Y. Morita, K. Murakami, M. Nagamatu, R. Nartallo, P. Nieminen, T. Nishimura, K. Ohtsubo, M. Okamura, S. O'Neale, Y. Oohata, K. Paech, J. Perl, A. Pfeiffer, M.G. Pia, F. Ranjard, A. Rybin, S. Sadilov, E. Di Salvo, G. Santin, T. Sasaki, N. Savvas, Y. Sawada, S. Scherer, S. Sei, V. Sirotenko, D. Smith, N. Starkov, H. Stoecker, J. Sulkimo, M. Takahata, S. Tanaka, E. Tcherniaev, E. Safai Tehrani, M. Tropeano, P. Truscott, H. Uno, L. Urban, P. Urban, M. Verderi, A. Walkden, W. Wander, H. Weber, J.P. Wellisch, T. Wenaus, D.C. Williams, D. Wright, T. Yamada, H. Yoshida, and D. Zschiesche. Geant4a simulation toolkit. *Nuclear Instruments and Methods in Physics Research Section A: Accelerators, Spectrometers, Detectors and Associated Equipment*, 506(3):250 – 303, 2003.

[AAA+06] J. Allison, K. Amako, J. Apostolakis, H. Araujo, P. Arce Dubois, M. Asai, G. Barrand, R. Capra, S. Chauvie, R. Chytracek, G. A. P. Cirrone, G. Cooperman, G. Cosmo, G. Cuttone, G. G. Daquino, M. Donszelmann, M. Dressel, G. Folger, F. Foppiano, J. Generowicz, V. Grichine, S. Guatelli, P. Gumplinger, A. Heikkinen, I. Hrivnacova, A. Howard, S. Incerti, V. Ivanchenko, T. Johnson, F. Jones, T. Koi, R. Kokoulin, M. Kossov, H. Kurashige, V. Lara, S. Larsson, F. Lei, O. Link, F. Longo, M. Maire, A. Mantero, B. Mascialino, I. McLaren, P. Mendez Lorenzo, K. Minamimoto, K. Murakami, P. Nieminen, L. Pandola, S. Parlati, L. Peralta, J. Perl, A. Pfeiffer, M. G. Pia, A. Ribon, P. Rodrigues, G. Russo, S. Sadilov, G. Santin, T. Sasaki, D. Smith, N. Starkov, S. Tanaka, E. Tcherniaev, B. Tome, A. Trindade, P. Truscott, L. Urban, M. Verderi, A. Walkden, J. P. Wellisch, D. C. Williams, D. Wright, and H. Yoshida.

Geant4 developments and applications. *IEEE Transactions on Nuclear Science*, 53(1):270–278, Feb 2006.

[AAA+16] J. Allison, K. Amako, J. Apostolakis, P. Arce, M. Asai, T. Aso, E. Bagli, A. Bagulya, S. Banerjee, G. Barrand, B.R. Beck, A.G. Bogdanov, D. Brandt, J.M.C. Brown, H. Burkhardt, Ph. Canal, D. Cano-Ott, S. Chauvie, K. Cho, G.A.P. Cirrone, G. Cooperman, M.A. Corts-Giraldo, G. Cosmo, G. Cuttone, G. Depaola, L. Desorgher, X. Dong, A. Dotti, V.D. Elvira, G. Folger, Z. Francis, A. Galoyan, L. Garnier, M. Gayer, K.L. Genser, V.M. Grichine, S. Guatelli, P. Guye, P. Gumplinger, A.S. Howard, I. Hivnov, S. Hwang, S. Incerti, A. Ivanchenko, V.N. Ivanchenko, F.W. Jones, S.Y. Jun, P. Kaitaniemi, N. Karakatsanis, M. Karamitros, M. Kelsey, A. Kimura, T. Koi, H. Kurashige, A. Lechner, S.B. Lee, F. Longo, M. Maire, D. Mancusi, A. Mantero, E. Mendoza, B. Morgan, K. Murakami, T. Nikitina, L. Pandola, P. Paprocki, J. Perl, I. Petrovi, M.G. Pia, W. Pokorski, J.M. Quesada, M. Raine, M.A. Reis, A. Ribon, A. Risti Fira, F. Romano, G. Russo, G. Santin, T. Sasaki, D. Sawkey, J.I. Shin, I.I. Strakovsky, A. Taborda, S. Tanaka, B. Tom, T. Toshito, H.N. Tran, P.R. Truscott, L. Urban, V. Uzhinsky, J.M. Verbeke, M. Verderi, B.L. Wendt, H. Wenzel, D.H. Wright, D.M. Wright, T. Yamashita, J. Yarba, and H. Yoshida. Recent developments in geant4. *Nuclear Instruments and Methods in Physics Research Section A: Accelerators, Spectrometers, Detectors and Associated Equipment*, 835:186 – 225, 2016.

[Bew05] B. Bewer. Development of a gain monitoring system for a neutron detector array. Master's thesis, University of Saskatchewan, Saskatoon, SK, Canada, 2005.

[BPIW09] B.E. Bewer, R.E. Pywell, R. Igarashi, and W.A. Wurtz. An led, fiber optic, gain monitoring system for a segmented scintillator array. *Nuclear Instruments and Methods in Physics Research Section A: Accelerators, Spectrometers, Detectors and Associated Equipment*, 608(3):417 – 423, 2009.

[BR97] Rene Brun and Fons Rademakers. Root an object oriented data analysis framework. *Nuclear Instruments and Methods in Physics Research Section A: Accelerators, Spectrometers, Detectors and Associated Equipment*, 389(1):81 – 86, 1997. New Computing Techniques in Physics Research V.

[Cha08] Daron Chabot. A pc-based data acquisition system for subatomic physics measurements. Master's thesis, University of Saskatchewan, Saskatoon, SK, Canada., 2008.

[Cho52] C. N. Chou. The nature of the saturation effect of fluorescent scintillators. *Phys. Rev.*, 87:904–905, Sep 1952.

[DH66] S. D. Drell and A. C. Hearn. Exact sum rule for nucleon magnetic moments. *Phys. Rev. Lett.*, 16:908–911, May 1966.

[DM95]   Tony Wilson Doug Murray, Glen Wright. Subatomic physics internal report 100: Lucid user's manual. Technical report, University of Saskatchewan, 1995. http://nucleus.usask.ca.

[Ger66]   S. B. Gerasimov. A Sum rule for magnetic moments and the damping of the nucleon magnetic moment in nuclei. *Sov. J. Nucl. Phys.*, 2:430–433, 1966. [Yad. Fiz.2,598(1965)].

[Kno10]   G.F. Knoll. *Radiation Detection and Measurement.* John Wiley and Sons, Hoboken, NJ, 3 edition, 2010.

[Kra88]   K. Krane. *Introductory Nuclear Physics.* Wiley, Hoboken NJ, 3 edition, 1988.

[Kuc10]   S. Kucker. *Photodisintegration of the Deuteron at 20MeV.* PhD thesis, University of Virginia, Charlottesville, VA, USA, 2010.

[LBE+97]   V. N. Litvinenko, B. Burnham, M. Emamian, N. Hower, J. M. J. Madey, P. Morcombe, P. G. O'Shea, S. H. Park, R. Sachtschale, K. D. Straub, G. Swift, P. Wang, Y. Wu, R. S. Canon, C. R. Howell, N. R. Roberson, E. C. Schreiber, M. Spraker, W. Tornow, H. R. Weller, I. V. Pinayev, N. G. Gavrilov, M. G. Fedotov, G. N. Kulipanov, G. Y. Kurkin, S. F. Mikhailov, V. M. Popik, A. N. Skrinsky, N. A. Vinokurov, B. E. Norum, A. Lumpkin, and B. Yang. Gamma-ray production in a storage ring free-electron laser. *Phys. Rev. Lett.*, 78:4569–4572, Jun 1997.

[Mav10]   Octavian Mavrichi. Photon flux monitor for a mono-energetic gamma ray source. Master's thesis, University of Saskatchewan, Saskatoon, SK, Canada, 2010.

[PMWW09]   R.E. Pywell, O. Mavrichi, W.A. Wurtz, and R. Wilson. Photon flux monitor for a mono-energetic gamma ray source. *Nuclear Instruments and Methods in Physics Research Section A: Accelerators, Spectrometers, Detectors and Associated Equipment*, 606(3):517 – 522, 2009.

[PSI+06]   R.E. Pywell, B.D. Sawatzky, J. Ives, N.R. Kolb, R. Igarashi, and W.A. Wurtz. Light output response of bc-505 liquid scintillator. *Nuclear Instruments and Methods in Physics Research Section A: Accelerators, Spectrometers, Detectors and Associated Equipment*, 565(2):725 – 730, 2006.

[Pyw17]   R. Pywell. Subatomic physics internal report 152: Bfroot: Blowfish root analysis package. Technical report, University of Saskatchewan, 2017. http://nucleus.usask.ca.

[SA01]   Michael Schwamb and Hartmuth Arenhvel. Off-shell effects in electromagnetic reactions on the deuteron. *Nuclear Physics A*, 696(3):556 – 580, 2001.

[Saw05]   B. Sawatzky. *A Measurement of the Neutron Asymmetry in d($\vec{\gamma}$,n)p Near Threshold.* PhD thesis, University of Virginia, Charlottesville, VA, USA, 2005.

[WAG+09]   Henry R. Weller, Mohammad W. Ahmed, Haiyan Gao, Werner Tornow, Ying K. Wu, Moshe Gai, and Rory Miskimen. Research opportunities at the upgraded his facility. *Progress in Particle and Nuclear Physics*, 62(1):257 – 303, 2009.

[WP16]   W. Wurtz and R. Pywell. Subatomic physics internal report 151: Rlucid: Lucid to root conversion package. Technical report, University of Saskatchewan, 2016. http://nucleus.usask.ca.

[Wur10]   W.A. Wurtz. *Photodisintegration of Lithium Isotopes*. PhD thesis, University of Saskatchewan, Saskatoon, SK, Canada, 2010.